Optics & Laser Technology 198 (2026) 114886

Contents lists available at ScienceDirect

Optics and Laser Technology

journal homepage: www.elsevier.com/locate/jolt

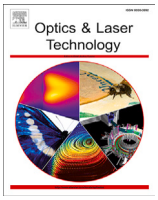

Full length article

# Dual-polarization interferometric sensing for independent characterization of surface and bulk layers

Ana Sánchez-Ramírez[a,b,*], José Manuel Luque-González[a], Laura Pérez-Sánchez[a,c], Miguel Barrio-Segura[a], Érika López-Arroyo[a,b], Rafael Godoy-Rubio[a], Claudio J. Oton[d], J. Gonzalo Wangüemert-Pérez[a,b], Iñigo Molina-Fernández[a,b]

[a] Photonics & RF Research Lab, Telecommunication Research Institute (TELMA), Universidad de Málaga, CEI Andalucía TECH, E.T.S.I. Telecomunicación, 29010 Málaga, Spain
[b] IBIMA Plataforma BIONAND, Parque Tecnológico de Andalucía, 29590 Málaga, Spain
[c] BIOHERENT, S.L., Calle Severo Ochoa, 34, 29590 Málaga, Spain
[d] Scuola Superiore Sant'Anna, Institute of Mechanical Intelligence, Via G. Moruzzi 1, 56124, Pisa, Italy

ARTICLE INFO

*Keywords:*
Photonic integrated biosensor
Dual-polarization
Coherent detection
Layer discrimination
Molecular binding
Background effects

ABSTRACT

Photonic integrated biosensors are a promising solution for biomarker detection in applications ranging from clinical diagnostics to food quality monitoring. However, their response is not only affected by molecular binding at the sensor surface, but also by bulk refractive index variations, background composition changes and temperature fluctuations. Most reported implementations cannot separate these effects, leading to inaccurate measurements. In this work, we present a fully integrated dual-polarization Mach-Zehnder interferometer with coherent detection, capable of distinguishing refractive index changes occurring at different distances above the waveguide surface, thereby enhancing sensor robustness. This is achieved through two separate measurements, one using the Transverse Electric (TE) mode and the other using the Transverse Magnetic (TM) mode. By exploiting their different evanescent field penetration depths and postprocessing the respective signals, we solve a system of equations to decouple surface and bulk contributions. Beyond refractive index sensing, this method could be extended to estimate additional parameters such as molecular layer thickness or temperature variations. The good agreement between simulation and experimental results confirms that the proposed sensor can effectively differentiate between contributions due to protein adsorption or biorecognition events within the 10 nm layer closest to the surface (surface effects) from bulk refractive index variations (background effects). To the best of our knowledge, this is the first demonstration of spatially resolved refractive index discrimination by an integrated photonic biosensor with coherent interrogation, highlighting its competitiveness against current state-of-the-art solutions.

## 1. Introduction

The development of highly sensitive and selective biosensors is crucial to address the increasing demands in medical diagnostics, environmental monitoring, and food quality control [1,2]. Biosensors based on photonic integrated circuits (PICs) have attracted significant attention due to their label-free detection, high sensitivity, miniaturization and their potential for multiplexing and large-scale production [3]. Among different material platforms, silicon nitride ($Si_3N_4$) stands out for its low optical losses, broad transparency window, and compatibility with complementary metal-oxide-semiconductor (CMOS) fabrication processes [4,5].

Unlike surface plasmon resonance (SPR)-based sensors, which offer enhanced sensitivity at the expense of increased optical losses [6], or microring-based resonant structures that are vulnerable to fabrication tolerances and typically require tunable lasers [7,8], Mach-Zehnder Interferometers (MZIs) offer accuracy and simplicity [9]. MZIs do not require wavelength sweeping and can operate with low-cost, fixed-wavelength laser sources, reducing system complexity and cost [10,11].

* Corresponding author at: Photonics & RF Research Lab, Telecommunication Research Institute (TELMA), Universidad de Málaga, CEI Andalucía TECH, E.T.S.I. Telecomunicación, 29010 Málaga, Spain.
*Email address:* anasanram@uma.es (A. Sánchez-Ramírez).

https://doi.org/10.1016/j.optlastec.2026.114886
Received 22 September 2025; Received in revised form 16 January 2026; Accepted 2 February 2026
Available online 13 February 2026

These architectures also support multiplexed configurations for the detection of multiple analytes [12,13] and coherent detection schemes, which reduce ambiguity and avoid sensitivity fading [14,15]. As a result, MZIs-based biosensors are particularly well suited for accurate measurements in complex biological environments.

All previously described architectures rely on the evanescent field principle, which occurs when matter interacts with an exponentially decaying localized optical field at the cladding interface of a dielectric waveguide [9]. This effect enables high sensitivity in waveguide-based photonic biosensors. However, in many single-layer functionalized biosensors based on self-assembled monolayers, silane chemistries or protein immobilization, the thickness of the biochemical recognition layer is typically only a few nanometers to a few tens of nanometers [16,17], which is much smaller than the evanescent-field penetration depth (usually 200–300 nm). In this thin-layer regime, the sensor response is strongly influenced by non-specific components in the sample, thermal drifts or background refractive index (RI) fluctuations. This directly undermines the robustness of the sensor, which ideally should respond exclusively to the target analyte [18,19]. By contrast, emerging biosensing platforms that use thicker two-dimensional material coatings (for example, graphene oxide, MXenes or $MoS_2$) may employ recognition layers with thicknesses comparable to or larger than the penetration depth [20,21]. In such configurations, the evanescent field interacts with the functional coating over a much larger distance and the sensor no longer operates in the thin-layer regime assumed in this work. These architectures require a different multilayer waveguide model and are therefore outside the specific scope of the present study.

In this work, we consider a thin effective surface layer. Under these conditions, while the affinity between the biomarker and the bioreceptor defines the chemical selectivity of the sensor, decoupling molecular binding from other undesired background effects is also critical for reliable measurements. To address this, both biochemical and optical strategies have been developed. Biochemical approaches such as blocking layers aim to minimize non-specific adsorption [22].

Optical strategies improve sensor performance by manipulating and analyzing guided light signals to reduce unwanted background effects [23]. These approaches often involve combining and comparing multiple optical modes, polarizations, or wavelengths. A common method is the use of reference channels—optical paths that do not interact with the analyte but instead measure environmental or bulk refractive index variations—allowing the cancellation of common-mode noise [24].

In this context, interferometric sensors typically follow two main approaches. One involves differential sensing, where two modes propagate simultaneously within the same waveguide and interfere to directly compare their phase changes. Bimodal waveguides, which use modes of different orders, represent a classical example of this differential approach, effectively canceling bulk RI fluctuations [25,26]. Similarly, some sensors utilize modes of different polarization: by combining TE and TM responses, they can reduce sensitivity to RI changes confined to a thin near-surface region (typically about 20–30 nm), thereby mitigating the impact of non-specific binding events [27]. However, differential sensors often face inherent limitations: i) reduced sensitivity compared to optimized single-mode interferometric designs with dedicated reference arms [25]; and ii) limited capability to resolve different physical parameter variations—such as RI variations in different regions or layer RI variation and thickness—since differential systems typically only yield a single effective measurement parameter [26].

Non-differential approaches, in contrast, treat each mode as an independent interferometer, allowing separate phase shift measurements. These designs can operate with a single mode, but recovering multiple physical parameters requires two or more sensing modes. In the case of Dual Polarization Interferometers (DPIs) [28], the two modes correspond to orthogonal polarizations (TE and TM). Both polarizations propagate through the same sensing and reference arms, but their phases are measured independently. This configuration enables simultaneous extraction of surface layer thickness and refractive index with enhanced robustness against environmental noise [28]. Beyond polarization diversity, using modes of different wavelengths or different mode orders is also a powerful strategy to increase the amount of retrievable information and improve sensor robustness. This can be demonstrated through a Young Interferometer, which allows simultaneous sensing across multiple wavelengths on a single platform [29]. Furthermore, hybrid approaches can combine differential polarization sensing (using TE and TM modes for sensing and reference) with multi-wavelength measurements to recover multiple parameters simultaneously [30].

Despite these advances, other system-level challenges persist: iii) off-chip multiplexing or demultiplexing of optical modes and wavelengths increases the complexity and footprint of devices; and iv) non-coherent detection schemes suffer from phase ambiguity and sensitivity fading. Among the solutions discussed, only one implementation [26] overcomes challenges (iii) and (iv) simultaneously through on-chip multiplexing and coherent readout. However, this solution relies on a differential bimodal architecture, which still suffers from intrinsic drawbacks, such as reduced sensitivity and the inability to extract multiple parameters. Consequently, no current implementation addresses all these issues simultaneously.

In this work, we primarily target limitations (i), (ii) and (iv), while partially mitigating limitation (iii). We address limitation (i), i.e., the sensitivity penalty of differential bimodal architectures by using a dual-polarization Mach–Zehnder interferometer on a $Si_3N_4$ platform. For each polarization, the device operates as a conventional MZI with separated sensing and reference arms, as illustrated in Fig. 1. Limitation (ii), namely the robust separation of bulk and surface responses under fabrication tolerances, is tackled at the waveguide and calibration level by a dual-polarization model and an equivalent-waveguide calibration protocol that separates bulk and surface refractive-index changes while compensating for geometric and refractive-index uncertainties. Limitation (iii), the reliance on off-chip mode/polarization multiplexing, is partially mitigated: in the present proof-of-concept the TE and TM states are still prepared off chip via time-division polarization control. However, once coupled into the chip, integrated Multimode Interferometers (MMIs) perform all interferometric splitting and combining, so that both polarizations propagate through the same physical paths and experience identical on-chip conditions. Finally, limitation (iv), related to phase ambiguity and sensitivity fading that arise when monitoring a single interferometric intensity output, is fully resolved through the coherent readout enabled by the on-chip 2x3 MMI. By providing three interference outputs with fixed relative phase offsets, I/Q reconstruction and continuous phase tracking become possible, supporting unambiguous phase retrieval and the extraction of two independent optical parameters (here, bulk and surface refractive-index changes) from a single device.

In the proof-of-concept implementation presented here, the temperature is stabilized experimentally and treated as a controlled variable rather than as an explicit sensing parameter. However, we note that the same dual-polarization framework can be configured to retrieve a different pair of variables (for example, temperature and a refractive-index-related quantity) in application-specific implementations.

By combining the simplicity of MZI-based systems with coherent detection, the proposed architecture significantly improves practical implementation, enabling layer discrimination and effectively decoupling bulk and surface effects. In particular, it allows distinguishing molecular interactions occurring within the first ten nanometers of the sensor surface, where biological recognition events take place, from the remaining cover. Notably, this approach complements, rather than replaces, conventional chemical techniques used to improve sensor robustness.

The remainder of the paper is organized as follows. First, we develop the mathematical framework for multi-parameter photonic biosensing, introducing the main analytical expressions and performance metrics necessary for layer discrimination. Next, we describe our dual-polarization Mach–Zehnder interferometer implementation and

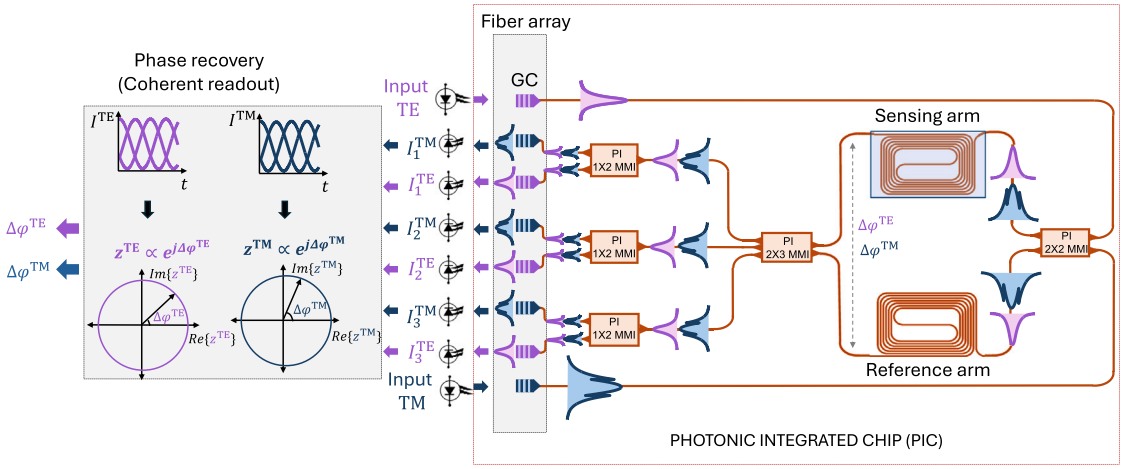


**Fig. 1.** Schematic of the proposed architecture for a dual polarization biosensor with layer discrimination capability, based on a MZI with coherent readout. Purple color represents TE polarization, whereas dark blue color represents TM polarization. If we focus on a single color (purple or blue) and disregard the 1×2 MMIs, the resulting architecture corresponds to a conventional biosensor based on a MZI with coherent readout operating with a single mode. Note that in this architecture MMIs are polarization insensitive (PI), while grating couplers (GCs) are polarization selective.

the design of the integrated sensing spiral. We then present experimental validation through bulk RI measurements using glycerol solutions, followed by a proof-of-concept demonstration of surface and bulk discrimination via alternating injections of glycerol and bovine serum albumin (BSA) solutions. The paper concludes with a summary of the main findings and a discussion of the advantages and improvements offered by the proposed sensing architecture.

## 2. Theoretical framework for layer discrimination

In this section, we present a comprehensive theoretical framework to describe the sensing process in multilayer environments. We start by introducing a simplified two-layer model that accounts for localized RI variations near the waveguide surface and in the bulk top cladding. We then show how this model reduces to the expression of classical bulk sensitivity under homogeneous RI variations. Finally, we introduce the matrix condition number as a key figure of merit to assess the stability and performance of the system.

In realistic biosensing scenarios, RI changes are often spatially non-uniform throughout the top cladding. For instance, molecular binding typically occurs near the waveguide surface, while the surrounding bulk fluid (e.g., buffer solution) remains approximately constant. This spatially structured behavior requires a multidimensional approach, beyond the conventional bulk sensitivity models that assume uniform RI changes. To address this complexity, the sensor cover is modeled as two different homogeneous regions, which are depicted in Fig. 2(a). A thin surface recognition layer lies directly on the waveguide, representing, for example, an adsorbed protein monolayer or functionalized molecular film. Although neither the bulk region nor the surface layer exhibits homogeneous behavior, we assume an idealized configuration for modeling purposes with a recognition layer of known thickness $d_p$ (e.g., 10 nm) and unknown average effective refractive index $n_p = n_c + \Delta n_p$. This layer is overlaid by the residual cover medium with refractive index $n_{rc} = n_c + \Delta n_{rc}$. Both bulk and surface layers exhibit small RI variations relative to a baseline refractive index $n_c$, which corresponds to the buffer solution covering the sensor (e.g., deionized water with $n_c = 1.32$ [31]). This baseline represents the refractive index of the pure buffer before any molecular binding or changes occur. Although the bulk residual cover is mainly the buffer solution, the refractive index $n_{rc}$ may slightly differ from the baseline $n_c$ due to the presence of free molecules, impurities, temperature fluctuations or small concentration changes in the bulk fluid ($\Delta n_{rc} \neq 0$). Thus, the total RI variation of the sensor cover ($\Delta n_c$) can be decomposed into two unknown components: $\Delta n_p$ in the surface layer ($R_p$) and $\Delta n_{rc}$ in the bulk residual region ($R_{rc}$).

It is also important to note that the proposed two-layer model is a deliberate simplification of biomolecular adsorption. In a realistic detection event, the surface region is not perfectly uniform and its optical response depends on both the adlayer refractive index and its thickness, as well as on hydration and partial filling within the near-surface region. In this work, we represent the surface contribution using a fixed, thin 10 nm virtual sensing region adjacent to the waveguide, as shown in Fig. 2(a). The choice of 10 nm is not intended to represent the physical thickness of the protein layer alone, but a representative effective thickness for typical biorecognition stacks at the sensor surface (surface chemistry/linker plus an adsorbed biomolecular layer). We define $\Delta n_p$ as the effective (field-weighted) refractive-index change within this region, capturing the net effect of the complete biorecognition stack. Because 10 nm is much smaller than the evanescent-field penetration depth of the guided modes (a few hundred nanometers), as illustrated in Fig. 2(b), the modal intensity varies only weakly across this region. As a result, the surface-induced phase shift contribution is well approximated by the average, field-weighted RI change within these first 10 nm. Under this definition, $\Delta n_p$ should be interpreted as a compact surface variable that already accounts for moderate adlayer inhomogeneity, partial filling and small thickness variations, rather than as a local refractive index at a specific height. This thin-adlayer treatment is consistent with common practice in evanescent-field biosensors [32] and with OWLS analyses, where hydrated nanolayers are widely described using effective homogeneous parameters despite underlying inhomogeneities [33,34].

To resolve the contributions from surface and bulk, we exploit the polarization-dependent behavior of optical modes. TE and TM modes exhibit distinct field profiles, as illustrated in Fig. 2(c) and (d), which can be quantified by comparing their evanescent field decay depths in the top cladding. Fig. 2(b) shows the normalized field amplitude $|E(y)|$, as a function of vertical distance from the waveguide surface for our nominal design geometry ($W = 1$ μm and $H = 300$ nm). From this analysis, we compute the $1/e$ field penetration depth ($\delta_p$), obtaining $\delta_p^{TE} = 187$ nm and $\delta_p^{TM} = 235$ nm. This difference indicates that the TE mode remains comparatively more confined near the surface, while the TM mode samples slightly deeper into the cladding. This relative contrast in field penetration enables the sensor to extract complementary information from surface and bulk refractive index variations by simultaneously tracking the phase response of both modes, thus enhancing the spatial resolution and robustness of the sensing platform. Although

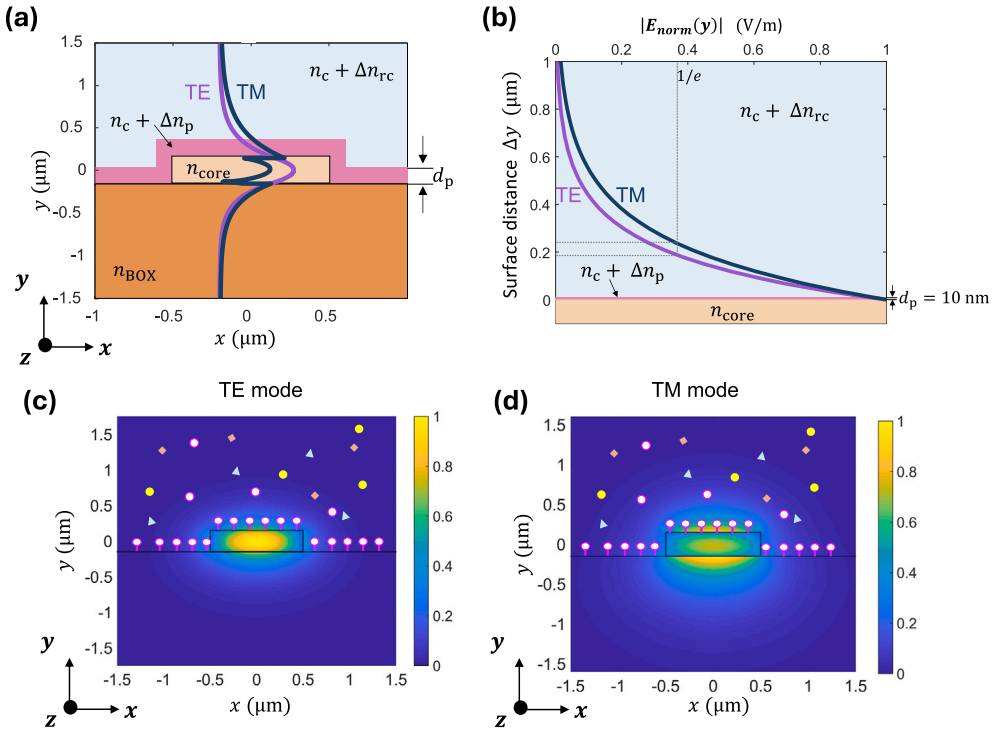


**Fig. 2.** (a) Two modes with different penetration depth (in this case, with different polarization state) propagating through the same sensing waveguide, thereby allowing layer discrimination (i.e., retrieving $\Delta n_{rc}$ and $\Delta n_p$); (b) Normalized $|E(y)|$ in the water cladding versus vertical distance for the fundamental TE and TM modes ($W$ = 1 μm, $H$ = 300 nm, $\lambda$ = 1310 nm, showing their different $1/e$ decay lengths ($\delta_p^{TE}$ = 187 nm and $\delta_p^{TM}$ = 235 nm); (c) $|E_x|$ field distribution for the fundamental TE mode in a $Si_3N_4$ waveguide at an operating wavelength of 1310 nm; (d) $|E_y|$ field distribution for the fundamental TM mode in a $Si_3N_4$ waveguide at an operating wavelength of 1310 nm.

this methodology can be extended to any number of regions and optical modes, in this work we focus on a simplified two-layer sensing structure:

$$\underbrace{\begin{bmatrix}\Delta\varphi^{TE}\\ \Delta\varphi^{TM}\end{bmatrix}}_{\overline{\Delta\varphi}} = \underbrace{\frac{2\pi L}{\lambda_0}}_{S_a}\underbrace{\overbrace{\begin{bmatrix}\frac{\partial n_{eff}}{\partial n_p}\Big|^{TE}_{n_p=1.32} & \frac{\partial n_{eff}}{\partial n_{rc}}\Big|^{TE}_{n_{rc}=1.32}\\ \frac{\partial n_{eff}}{\partial n_p}\Big|^{TM}_{n_p=1.32} & \frac{\partial n_{eff}}{\partial n_{rc}}\Big|^{TM}_{n_{rc}=1.32}\end{bmatrix}}^{\overline{\overline{S}}_{WG}}}_{\overline{\overline{S}}_T}\underbrace{\begin{bmatrix}\Delta n_p\\ \Delta n_{rc}\end{bmatrix}}_{\overline{\Delta n}}. \quad (1)$$

In this expression, $\overline{\Delta\varphi}$ is a vector containing the phase shifts for each mode (TE or TM) and $\overline{\Delta n}$ is a vector representing the RI variations in each defined region: the protein layer ($\Delta n_p$) and the remaining cover ($\Delta n_{rc}$). The total sensitivity matrix $\overline{\overline{S}}_T$ is the product of two terms. The first term is the architecture sensitivity, $S_a = 2\pi L/\lambda_0$. Here, $L$ is the length of the sensing waveguide and $\lambda_0$ is the operating wavelength. The second term is the waveguide sensitivity matrix, $\overline{\overline{S}}_{WG}$, which quantifies how changes in RI within each layer affect the effective refractive index $\Delta n_{eff}$ of each guided mode. The elements of this matrix can be derived either using full numerical simulations of the perturbed structures or, under the perturbative approximation, from overlap integrals of the unperturbed field profiles [35,36]. The refractive index variations in both the recognition layer ($\Delta n_p$) and the bulk remaining cover ($\Delta n_{rc}$) are expected to be relatively small. Specifically, $\Delta n_p$ typically remains below approximately 0.13 RIU, corresponding to protein layers with refractive indices below 1.45 [37,38]. Similarly, variations in the bulk cover refractive index $\Delta n_{rc}$ are also expected to be minor, generally not exceeding 0.1 RIU. Given these limited variations, the perturbative approximation remains valid, supporting the use of a linear sensitivity model.

To quantify how strongly each mode interacts with the surface layer, we define the surface overlap factor ($\eta^i$) as the relative power fraction in the surface recognition layer ($R_p$) with respect to the power within the entire cover ($R_{cover}$):

$$\eta^i = \frac{\int\int_{R_p} |\overline{E}^i(x,y)|^2 dxdy}{\int\int_{R_{cover}} |\overline{E}^i(x,y)|^2 dxdy}, \quad (2)$$

where $\overline{E}^i(x,y)$ is the transverse electric field profile of the unperturbed mode $i$ (TE or TM) when the sensing waveguide is covered only by the reference buffer of refractive index $n_c$ = 1.32. Here, the cover region ($R_{cover}$) encompasses both the surface recognition layer ($R_p$) of thickness $d_p$ = 10 nm and the remaining bulk medium above it ($R_{rc}$). In the simulations, the upper limit of the cover region is set by the top of the numerical window. This window is chosen large enough to ensure that the modal field has decayed and the result is insensitive to the exact position of this boundary. Under the first-order perturbation model used in this work, the surface overlap factors $\eta^i$ can be used to distribute the conventional bulk sensitivity $S^i_{wg,B}$ (defined for a homogeneous RI change over $R_{cover}$) into two partial contributions: the surface-region term, $S^i_{wg,B}\cdot\eta^i$, and the remaining-cover term, $S^i_{wg,B}\cdot(1-\eta^i)$. The full derivation of this factorization and its relation to Eq. (1) is provided in Appendix A. Thus, the waveguide sensitivity matrix in Eq. (1) can be written as:

$$\overline{\overline{S}}_{WG} = \underbrace{\begin{bmatrix}S^{TE}_{wg,B} & 0\\ 0 & S^{TM}_{wg,B}\end{bmatrix}}_{\overline{\overline{S}}_{WG,B}}\cdot\underbrace{\begin{bmatrix}\eta^{TE} & 1-\eta^{TE}\\ \eta^{TM} & 1-\eta^{TM}\end{bmatrix}}_{\overline{\overline{\eta}}}. \quad (3)$$

Here, $S^{TE}_{wg,B}$ and $S^{TM}_{wg,B}$ are the waveguide bulk sensitivities of each polarization mode, defined as their effective index response to uniform

RI changes across the entire cover region. The matrix, $\overline{\overline{\eta}}$, on the other hand, encodes the spatial distribution of the interaction of each mode with the layered cover.

The decomposition of Eq. (3) not only offers conceptual clarity by separating the waveguide bulk optical response from spatial field distribution effects but also simplifies the calibration procedure. On the one hand, two of the four parameters, $S^{\mathrm{TE}}_{\mathrm{wg,\,B}}$ and $S^{\mathrm{TM}}_{\mathrm{wg,\,B}}$, can be independently obtained using standard bulk RI measurements, where a homogeneous RI change is applied to both defined regions ($\Delta n_{\mathrm{p}} = \Delta n_{\mathrm{rc}} = \Delta n_{\mathrm{c}}$). Under this condition, Eq. (1) simplifies to [37]:

$$\overline{\Delta\varphi} = S_{\mathrm{a}} \cdot \overline{\overline{S}}_{\mathrm{WG,\,B}} \cdot \overline{\Delta n}. \tag{4}$$

This corresponds precisely to the conventional bulk sensitivity model, where each polarization mode responds independently to the global RI change in the cover ($\Delta n_{\mathrm{c}}$). Thus, the overall phase shift for each mode is given by [37]:

$$\Delta\varphi^{i} = S^{i}_{\mathrm{T}} \cdot \Delta n_{\mathrm{c}} = S_{\mathrm{a}} \cdot S^{i}_{\mathrm{wg,\,B}} \cdot \Delta n_{\mathrm{c}}, \tag{5}$$

where $S^{i}_{\mathrm{T}}$ represents the total system sensitivity for mode $i$ (TE or TM), combining both the architecture sensitivity $S_{\mathrm{a}} = 2\pi L/\lambda_0$ and the waveguide bulk sensitivity. Thus, $S^{i}_{\mathrm{T}}$ quantifies the total phase response of the sensor to uniform RI variations across the entire cover region.

On the other hand, full characterization of $\overline{\overline{S}}_{\mathrm{WG}}$ also requires independent measurement of $\eta^{\mathrm{TE}}$ and $\eta^{\mathrm{TM}}$, e.g., through controlled deposition of a surface layer with known thickness ($d_{\mathrm{p}}$) and refractive index ($n_{\mathrm{p}}$). However, this method is experimentally challenging and subject to uncertainties in layer uniformity. Therefore, we adopt a hybrid strategy: we determine $S^{\mathrm{TE}}_{\mathrm{wg,\,B}}$ and $S^{\mathrm{TM}}_{\mathrm{wg,\,B}}$ experimentally and infer the values of $\overline{\overline{\eta}}$ from simulations, thereby completing the system characterization.

Ideally, optimal system performance would be achieved if each optical mode interacted exclusively with a single region of the sensing structure, i.e., if mode TE probed only the surface layer ($\eta^{\mathrm{TE}} = 1$) and mode TM only the bulk ($\eta^{\mathrm{TM}} = 0$). In this idealized scenario, the overall system sensitivity matrix $\overline{\overline{S}}_{\mathrm{T}}$ would be diagonal, and each measurement channel would provide an independent and direct estimate of the RI variation in its corresponding region.

In practice, due to the evanescent nature of the field profiles of guided modes, it is not possible for every mode to interact with only one layer. Consequently, each measured phase shift reflects a linear combination of refractive index variations from both the surface and bulk layers. Therefore, the sensitivity matrix $\overline{\overline{S}}_{\mathrm{T}}$ is generally non-diagonal, and retrieving the individual RI changes requires inversion of the full matrix. The stability and quality of the inversion process are characterized by the condition number of the sensitivity matrix, defined as [39,40]:

$$\kappa(\overline{\overline{S}}_{\mathrm{T}}) = ||\overline{\overline{S}}_{\mathrm{T}}|| \cdot ||\overline{\overline{S}}_{\mathrm{T}}^{-1}||, \tag{6}$$

where $||\cdot||$ represents the 2-norm of a matrix. This condition number bounds the relative error propagation from phase shift measurements to RI variations as [39,40]:

$$\varepsilon_{\overline{\Delta n}} \le \kappa(\overline{\overline{S}}_{\mathrm{T}}) \cdot \varepsilon_{\overline{\Delta\varphi}}. \tag{7}$$

In this expression, $\varepsilon_{\overline{\Delta n}}$ and $\varepsilon_{\overline{\Delta\varphi}}$ are the relative errors in the retrieved RI variations and in the phase measurements, respectively. According to this expression, a high condition number indicates a poorly conditioned system, in which even small measurement noise can lead to large errors in the retrieved RI values [41].

Importantly, since the system sensitivity matrix is related to the waveguide sensitivity matrix by the scalar interferometric architecture sensitivity ($\overline{\overline{S}}_{\mathrm{T}} = S_{\mathrm{a}} \cdot \overline{\overline{S}}_{\mathrm{WG}}$), the condition number depends solely on $\overline{\overline{S}}_{\mathrm{WG}}$:

$$\kappa(\overline{\overline{S}}_{\mathrm{T}}) = \kappa(S_{\mathrm{a}} \cdot \overline{\overline{S}}_{\mathrm{WG}}) = \kappa(\overline{\overline{S}}_{\mathrm{WG}}). \tag{8}$$

This means that $S_{\mathrm{a}}$ does not affect the numerical stability of the inversion. Thus, minimizing $\kappa(\overline{\overline{S}}_{\mathrm{WG}})$ through careful waveguide design directly reduces noise amplification and enhances the accuracy and robustness of multilayer refractive index sensing. A more rigorous, covariance-based error-propagation analysis, explicitly relating the TE/TM phase noise to the uncertainties in $\Delta n_{\mathrm{p}}$ and $\Delta n_{\mathrm{rc}}$ is provided in Appendix B.

## 3. Implementation of dual-polarization photonic biosensor with layer discrimination capabilities

The proposed dual polarization sensing system with layer discrimination capabilities is schematically illustrated in Fig. 1, where the purple color represents TE polarization and the dark blue color represents TM polarization. As shown, modes with different polarizations are coupled into the photonic chip using two different types of grating couplers (GCs), each designed for a specific polarization. These modes are then recombined using a 2×2 multimode interferometer (MMI), which splits both signals into the sensing and reference arms. In the sensing arm, both guided modes interact with the sample, as shown in Fig. 2(a), inducing a phase shift for each polarization ($\Delta\varphi^{\mathrm{TE}}$ and $\Delta\varphi^{\mathrm{TM}}$) relative to the reference arm, which remains isolated from the sample. The phase-shifted signals are recombined using a coherent detection system, implemented with a 2×3 MMI, and further split into two outputs using a 1×2 MMI. Each of the resulting signals is then decoupled from the chip via a polarization-selective surface grating coupler. This component not only efficiently decouples the desired polarization, but also filters out the undesired polarization component to ensure a high extinction ratio and signal purity. Finally, the six optical outputs are converted into photocurrents using six different photodetectors.

In this architecture, the optical fields from the sensing and reference arms are recombined in a 2×3 MMI coupler that operates as a 120° optical hybrid, enabling coherent detection. The MMI produces three interference outputs with nominal relative phase offsets of approximately 0°, 120° and 240°, so that the three detected output signals ($I_1, I_2, I_3$) can ideally be regarded as three phase-shifted samples of the same interference fringe [15]. As a result, the three intensities provide three independent linear combinations of the in-phase and quadrature components (I, Q) of the complex interferometric signal $z = I + jQ$, and $z$ can be reconstructed from ($I_1, I_2, I_3$) through a suitable linear transformation.

In practice, fabrication tolerances introduce amplitude and phase imbalances in the 2×3 MMI, so that the reconstructed trajectory in the I-Q plane during a pure phase variation is slightly elliptical rather than perfectly circular. To compensate for these non-idealities, a short experiment is carried out by flowing a controlled calibration solution (for example, a glycerol solution in buffer) through the sensing channel, so that the interferometric phase $\Delta\varphi$ evolves smoothly and the corresponding calibration trace is recorded. From this dataset, we estimate a linear 2×3 reconstruction matrix and an offset vector (equivalently, an affine "ellipse-to-circle" correction) such that the calibrated in-phase and quadrature components are obtained as [14,42]

$$\begin{aligned} I &= m_{11}\, I_1 + m_{12}\, I_2 + m_{13}\, I_3 + c_1, \\ Q &= m_{21}\, I_1 + m_{22}\, I_2 + m_{23}\, I_3 + c_2. \end{aligned} \tag{9}$$

Once this coherent-readout calibration has been performed, any new triplet of measured intensities ($I_1, I_2, I_3$) is transformed using the same linear relations to obtain the complex signal, $z = I + jQ$. The interferometric phase is then directly obtained from the argument of $z$ and used

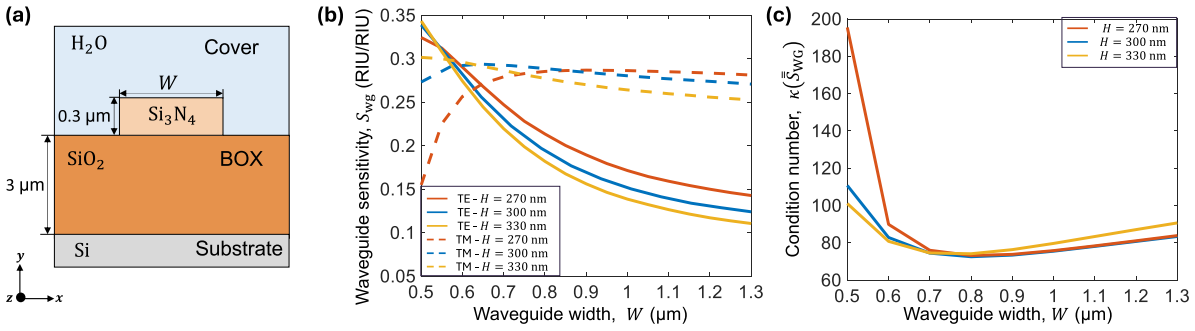


**Fig. 3.** (a) Cross-section of the photonic waveguide geometry used for the sensor design. (b) Simulated bulk waveguide sensitivities as a function of waveguide width $W$ for three core thicknesses ($H = 270$ nm, $H = 300$ nm and $H = 330$ nm). (c) Corresponding condition numbers $\kappa(\bar{\bar{S}}_{WG})$ of the dual-polarization waveguide sensitivity matrix versus $W$ for the same thicknesses, assuming a 10 nm surface biorecognition layer on the sensor.

in our sensing model for unambiguous determination of phase shifts and thereby for the accurate retrieval of the refractive index changes.

We will next focus on the design and simulated performance of the sensing waveguide spiral, which is the most important and challenging component of the system. Although the design of other photonic components—such as MMIs and gratings—is not discussed in this section, it is important to note that MMIs are designed to be polarization insensitive (PI), i.e., they must operate equally well for both TE and TM polarizations. In contrast, gratings are polarization-selective: they must be optimized to provide high coupling efficiency for the target polarization while minimizing coupling for the orthogonal one.

The spirals are designed for an operating wavelength of 1310 nm based on the commercial silicon nitride platform provided by Cornerstone. This platform includes a 300 nm $Si_3N_4$ layer ($n_{Si_3N_4} = 2.03354$), a 3 μm buried oxide (BOX) layer ($n_{BOX} = 1.4468$), and a 2 μm silicon dioxide top cladding layer ($n_{SiO_2} = 1.4468$) [43,44]. All these layers are deposited over a silicon substrate ($n_{Si} = 3.5003$) [45]. Fabrication is carried out using deep-ultraviolet projection lithography followed by reactive ion etching steps, enabling scalable and cost-effective production [43].

The geometry of the sensing waveguide is illustrated in Fig. 3(a), where the removal of the upper cladding is also shown. This uncovered section, referred to as the sensing window, enables direct interaction between the guided optical field and the external medium through the evanescent field. Under typical experimental conditions, the sensing window is covered with an aqueous solution, such as a buffer, with a refractive index around $n_c = n_{H_2O} = 1.32$ [31].

In this context, the waveguide width ($W$) is the key design parameter as it strongly influences both mode confinement and the extent of the evanescent field with the surrounding medium. The waveguide supports TE and TM polarizations, each exhibiting different sensitivity behaviors as plotted in Fig. 3(b). For the nominal thickness imposed by the foundry fabrication process, $H = 300$ nm, the TE mode bulk sensitivity significantly increases as the width decreases. In contrast, the sensitivity of the TM mode remains relatively constant over the same width range, as its field distribution is less dependent on lateral confinement.

These sensitivity curves reflect how each polarization mode responds to variations in the surrounding medium. However, as previously mentioned, achieving high sensitivity for each mode is not enough for effective multilayer discrimination. Instead, the critical factor is ensuring that the sensitivity matrix is well conditioned, which requires that the modes exhibit sufficiently distinct responses to allow reliable separation of surface and bulk effects. Fig. 3(c) presents the condition number values assuming a thickness of the protein layer of $d_p = 10$ nm. It shows that the condition number reaches a minimum value near a waveguide width of $W = 0.8$ μm. This minimum reflects the fact that, at this intermediate width, the TE mode remains comparatively more confined while the TM mode penetrates deeper into the cover, so their relative surface and bulk sensitivities differ more strongly and the dual-polarization

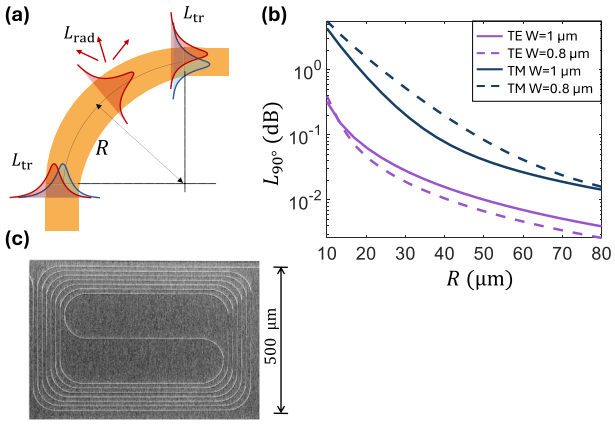


**Fig. 4.** (a) Generic 90° bent waveguide. Losses come from radiation in the curve and the mode mismatch in the transition between straight and bent sections; (b) Total losses per 90° bend for both polarizations, simulated at a wavelength of 1310 nm for two different waveguide widths ($W = 1$ μm and $W = 0.8$ μm); (c) SEM picture of the fabricated sensing spiral, with a total waveguide length of 9 mm compactly integrated within an area of $800 \times 500$ μm$^2$.

inversion is better conditioned, improving the robustness of the retrieved surface and bulk contributions.

To account for realistic process deviations, the analyses in Fig. 3 are carried out for three core thicknesses, $H = 270$ nm, 300 nm and 330 nm, corresponding to the maximum ±30 nm thickness tolerance specified by the foundry around the nominal value [43]. Although TE and TM are both affected by thickness variations, close to our design region ($W = 1$ μm) both the bulk sensitivity and the matrix condition number, $\kappa(\bar{\bar{S}}_{WG})$, vary slightly over the considered thickness range. These results confirm that, within the expected fabrication tolerances, the performance and numerical stability of the proposed dual-polarization sensing scheme are not compromised.

To ensure sensor compactness while maintaining reliable operation, a conservative $L = 9$ mm device length was chosen, limiting waveguide propagation losses. The waveguide is laid out in a spiral geometry, corresponding to an architecture sensitivity of $S_a = 43167$ rad/RIU for an operating wavelength of 1310 nm. This approach allows long interaction lengths to be integrated into a limited chip area. In particular, a Manhattan-style spiral is used [46,47], where straight waveguide sections are connected by a 90° bend with a constant curvature radius, as shown in Fig. 4(a). However, such bends introduce curvature losses, which must be carefully considered during the design process. The total loss introduced by a 90° bend is defined as:

$$L_{90}(\mathrm{dB}) = L_{\mathrm{rad}}(\mathrm{dB}) + 2 \cdot L_{\mathrm{trans}}(\mathrm{dB}), \tag{10}$$

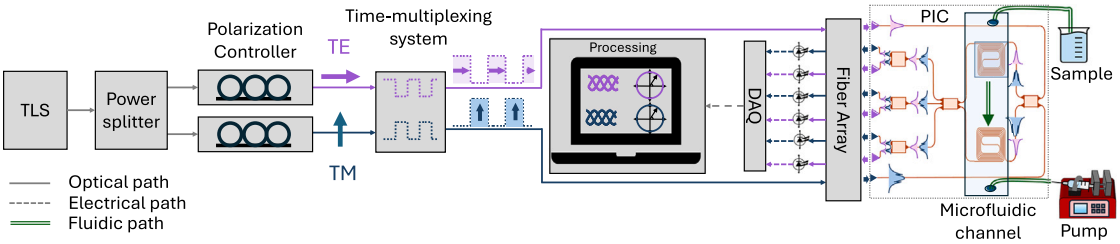


**Fig. 5.** Schematic of the measurement setup for dual-polarization sensing with layer discrimination capability. Input signal is generated by a tunable laser source (TLS) and divided into two signals, each with independent polarization control to excite TE (purple color) and TM (dark blue color) modes. These signals are time-multiplexed and coupled into the chip through a fiber array.

where $L_{rad}$ represents the radiation loss associated with a 90° bend, and $L_{trans}$ corresponds to the mode mismatch loss occurring at the transition between straight and bent waveguide sections. For 90° bends with constant radius $R$, $L_{rad}$ can be expressed as:

$$L_{rad}(\text{dB}) = \frac{\pi}{2} \cdot R(\mu\text{m}) = \cdot\alpha_{rad}(\text{dB}/\mu\text{m}), \tag{11}$$

where $\alpha_{rad}$ is the mode radiation loss coefficient, expressed in dB/μm.

The dependence of total bend loss ($L_{90}$) on the bend radius is shown in Fig. 4(b) for waveguide widths of $W = 0.8$ μm and $W = 1$ μm. Based on this analysis, a minimum bend radius of $R = 75$ μm is selected to ensure negligible curvature losses for both TE and TM modes.

Although matrix condition number analysis indicates that the optimal width is approximately 0.8 μm, possible overetching during the opening step of the sensing window could unintentionally reduce the width of the waveguide [26]. Narrower waveguides result in increased bending losses for the TM mode and are less tolerant to fabrication errors, which can significantly degrade optical performance. To mitigate these risks, a wider nominal waveguide is chosen. However, this width cannot be arbitrarily increased, as maintaining single-mode operation for each polarization is essential to minimize modal crosstalk and ensure accurate sensing. The single-mode cutoff waveguide width for this platform is approximately 1.2 μm; therefore, a conservative nominal width of $W = 1$ μm is selected. This choice balances robustness against fabrication variations, bending loss reduction, and preservation of monomode behavior, ensuring reliable sensor performance. A scanning electron microscope (SEM) image of the final fabricated spiral waveguide is shown in Fig. 4(c), demonstrating the compact integration of a 9 mm-length biosensor.

## 4. Experimental validation

The experimental setup used in this work is illustrated in Fig. 5. A tunable laser source (TLS) operating at 1310 nm (Model: Santec TSL-570) provides the optical input signal, which is equally divided into two branches using a fiber-based 50:50 power splitter (BXC25). Each branch is connected to a manual polarization controller (Thorlabs FPC562) to independently control the polarization state of the two input signals. These signals, corresponding to TE and TM modes, are coupled into the photonic chip with a 29° angle-polished fiber array (O/E Land) via grating couplers (GCs). This specific angle was chosen to optimize the coupling efficiency of the GCs.

The chip is operated in a time-division multiplexing (TDM) scheme by two fiber variable optical attenuators (VOAs) at the input. The VOAs are controlled by complementary 0–5 V square waves at 100 Hz, ensuring that only one polarization (TE or TM) is injected during each 5 ms half-period. The sensor outputs and the two VOA control signals are acquired simultaneously at 31.25 kS/s per channel. To reduce data volume while preserving the temporal resolution required by the TDM scheme, we apply a software block-averaging of $N_{avg} = 50$ consecutive samples on each channel and only store these averaged values. In post-processing, the stored VOA traces are thresholded at 75% of the 0–5 V range to build TE/TM masks. To ensure signal integrity, the first and last stored points of each half-period are discarded, providing a short guard interval around the switching edges. As a result, only the central, steady part of each TE and TM window is used for phase reconstruction.

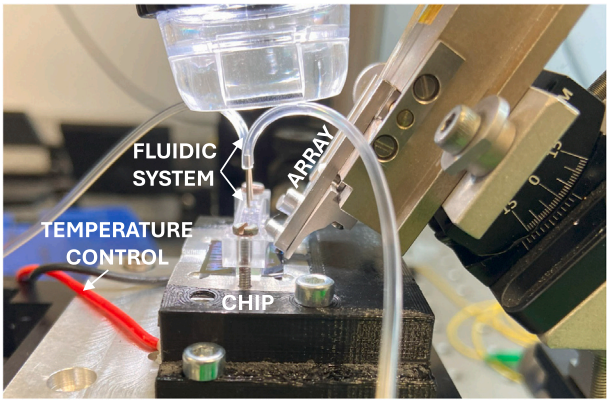


**Fig. 6.** Actual experimental setup. The fiber array is visibly aligned with the photonic chip, and a microfluidic channel is placed on top to deliver the sample across the sensing spirals.

Residual effects of the TDM and finite VOA extinction were characterized in dedicated calibration measurements under single-polarization injection. We measured ON/OFF extinctions of –15.5 dB for TE and –14 dB for TM. Furthermore, we quantified the polarization leakage into the orthogonal detection block: in a TE-only measurement, the TE-to-TM mixing ratio was approximately –25.6 dB (≈ 0.3% of the useful signal), and in a TM-only measurement, the TM-to-TE mixing ratio was –36.9 dB (≈ 0.02%). Consequently, any cross-contamination is well below 1% of the signal power, having a negligible impact on the reconstructed phases.

Once the light has been injected into the chip, it propagates through the interferometric sensing architecture. At the output, the six optical signals—three for each polarization state—are coupled out of the chip by using the same fiber array and carried to six photodetectors (three Thorlabs PDA10CS-EC and three Thorlabs PDA20CS). The analog signals are digitized by a 16-bit DAQ module (NI USB-6210) and further processed with a custom MATLAB routine for calibration and phase extraction. This dual-polarization coherent readout scheme allows independent tracking of the phase shift experienced by fundamental TE and TM modes as they propagate through sensing and reference spirals. These phase shifts enable the reconstruction of RI variations occurring at two different depths: one close to the surface and the other in the bulk of the sample, thereby providing the sensor with the ability to discriminate between layers.

The sensing spiral is covered by a custom-designed PDMS microfluidic flow cell and sealed with a methacrylate holder to ensure robust and leak-free operation, as shown in Fig. 6. During experiments, liquid

samples were introduced into the flow cell using a withdrawal pump (New Era NE-1000) operating at a constant flow rate of 40 μL/min, which ensures stable delivery across the sensing region.

Furthermore, to reduce thermal fluctuations that could affect the phase measurements, the photonic chip is placed on a temperature-controlled stage. This stage consists of a Thorlabs TECH3S thermoelectric cooler (TEC) module, driven by an MTD1020T TEC driver mounted on an MTDEVAL1 evaluation board, with a TH10K thermistor providing real-time temperature feedback. The system is regulated by the MTD1020T TEC driver, maintaining the chip at a constant temperature throughout the experiments. The constant temperature is set to the ambient temperature measured at the beginning of each experiment using a calibrated thermometer. In this setup, the long-term temperature standard deviation over the typical duration of the sensing experiments (several hours) is approximately $2.6 \cdot 10^{-3}$ °C. An independent phase-vs-temperature calibration yields thermal phase sensitivities $S_{\mathrm{th}}^{\mathrm{TE}} \approx 0.7$ rad/°C and $S_{\mathrm{th}}^{\mathrm{TM}} \approx 1$ rad/°C. Consequently, temperature-induced phase excursions remain on the order of $10^{-3}$ rad. In addition, a simple linear baseline removal is applied in software to suppress residual slow drifts, so that the remaining phase noise is dominated by short-term fluctuations. As a result, the residual thermal noise floor remains much smaller than the phase changes associated with the bulk and surface refractive-index steps analyzed in this work and does not limit the discrimination performance.

Three independent subsections are presented below. First, a conventional bulk characterization of multiple chips under controlled ambient temperature conditions is performed to evaluate sensor operation for TE and TM modes independently, determine their bulk sensitivities, and assess inter-chip reproducibility. Second, a per-chip calibration protocol is explained to extract the full sensitivity matrix required for layer discrimination; this calibration must be repeated at the beginning of each proof-of-concept experiment. Third, a proof-of-concept is demonstrated on a specific chip. The first two injections of this experiment are used to perform the calibration described in the second subsection, while the remaining data are used to retrieve RI variations in both surface and bulk regions.

### 4.1. Sensor characterization with glycerol solutions

This subsection presents the conventional bulk characterization of multiple chips, evaluating TE and TM modes independently to determine their bulk sensitivities ($S_{\mathrm{T}}^{\mathrm{TE}}$ and $S_{\mathrm{T}}^{\mathrm{TM}}$) and assess reproducibility across different chips. By flowing homogeneous glycerol-water solutions of known refractive index over the sensing region, we can monitor the phase shifts induced in both polarization modes under controlled conditions. Specifically, we used glycerol concentrations of 3%, 6%, 9%, and 12% (w/w), which correspond to RI variations in the cladding region of $\Delta n_{\mathrm{c}} = 3.4$ mRIU, 6.9 mRIU, 10.4 mRIU and 14.1 mRIU, respectively [48,49]. These values are relative to the baseline refractive index of pure water ($n_{\mathrm{c}} = 1.32$), which acts as a buffer, and ensures that the cover refractive index remains homogeneous throughout the measurement. Under these conditions, the two-layer model effectively reduces to a single-layer case, as discussed in the theoretical section, enabling direct extraction of bulk sensitivities.

Glycerol–water solutions were stored in the same temperature-controlled laboratory as the setup to ensure thermal equilibrium with the TEC-stabilized chip. Given the small difference in thermo-optic coefficients between water and the mixtures ($|\Delta(dn/dT)| \approx 10^{-5}$ RIU/°C), even a conservative 1 °C temperature difference yields a negligible error of $|\Delta n_{\mathrm{T}}| \lesssim 10^{-5}$ RIU [50,51]. This deviation corresponds to < 0.3% of the smallest calibration step, confirming that residual temperature mismatches do not affect calibration accuracy.

Rather than showing the temporal response of a single sensor, Fig. 7(a) summarizes the bulk characterization across seven chips by plotting the phase shift as a function of RI variation for TE and TM modes. For clarity, the average response is shown rather than individual curves, and error bars represent inter-chip variability (± 2 standard deviations, ≈ 95% confidence interval). Based on these measurements, bulk sensitivities were extracted for each of the seven chips. Fig. 7(b) and (c) presents these sensitivities as scatter plots for TE and TM modes, respectively, with error bars indicating the same inter-chip variability as in Fig. 7(a). This representation provides a consistent and robust view of system reproducibility and the stability of the bulk sensitivity for both polarizations.

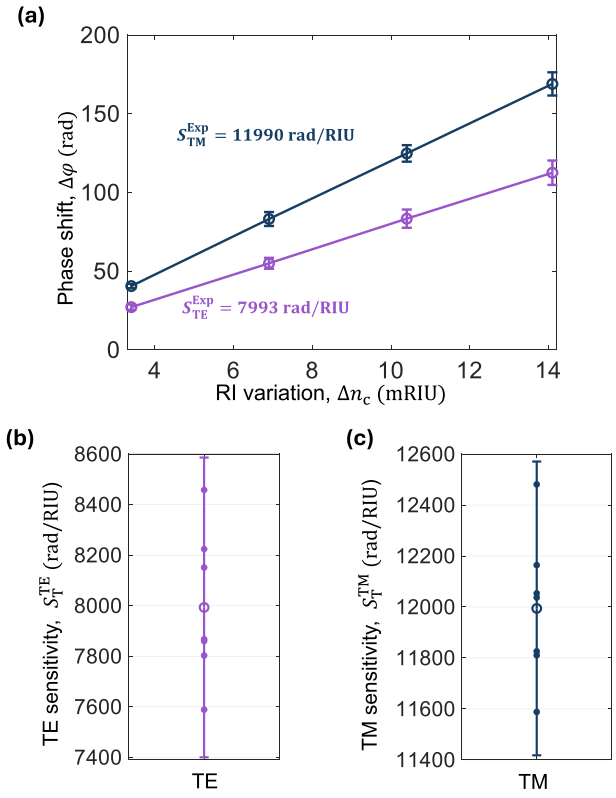


**Fig. 7.** Bulk characterization of TE and TM modes across seven photonic chips: (a) Measured phase shift versus bulk refractive index variation for TE and TM modes across seven chips; error bars represent ±2 standard deviations across chips (≈ 95% confidence interval); (b) Scatter plot of measured bulk sensitivities for TE mode; (c) Scatter plot of measured bulk sensitivities for TM mode.

The resulting phase shifts for both TE and TM modes in Fig. 7(a) exhibited a linear dependence on the bulk refractive index, as expected, and their responses were sufficiently different. This confirms that the photonic chip enables reliable and decoupled measurement in both polarizations under bulk sensing conditions. The bulk sensitivities, averaged across the seven chips, were approximately $S_{\mathrm{T}}^{\mathrm{TE}} = 7993$ rad/RIU for the TE mode and $S_{\mathrm{T}}^{\mathrm{TM}} = 11990$ rad/RIU for the TM mode, which correspond to waveguide sensitivities of $S_{\mathrm{wg,B}}^{\mathrm{TE}} = 0.1852$ RIU/RIU and $S_{\mathrm{wg,B}}^{\mathrm{TM}} = 0.2778$ RIU/RIU. These experimental values show reasonable agreement with simulated sensitivities shown in Fig. 3(b), which predict $S_{\mathrm{wg,B}}^{\mathrm{TE}} = 0.15$ RIU/RIU and $S_{\mathrm{wg,B}}^{\mathrm{TM}} = 0.28$ RIU/RIU for the nominal waveguide width of $W = 1$ μm. The observed deviations are attributed primarily to fabrication-related factors such as dimensional tolerances and overetching due to the sensing window opening, which can alter the effective waveguide geometry and, consequently, the measured sensitivities. This bulk characterization achieves two specific purposes. First, it confirms that the sensor yields distinct and measurable responses for both TE and TM modes. Second, it provides a benchmark for typical experimental sensitivity values and their variability across chips—typically within ±4%—highlighting the importance of individual, per-chip-specific calibration to improve the precision of RI retrieval during sensing experiments.

### 4.2. Sensitivity matrix calibration protocol

This section describes the per-chip calibration protocol developed to extract the full sensitivity matrix necessary for accurate layer discrimination. This protocol is performed at the beginning of each proof-of-concept experiment to account for chip-specific variations. To resolve the four unknown sensitivity coefficients in the matrix presented in Eq. (3)—i.e. $S^{TE}_{wg,B}$, $S^{TM}_{wg,B}$, $\eta^{TE}$, and $\eta^{TM}$—we follow a two-step calibration procedure under controlled conditions.

**Step 1: experimental bulk sensitivity calibration.** In this step, the entire sensing region is exposed to a homogeneous fluid of known refractive index (i.e., $\Delta n_p = \Delta n_{rc} = \Delta n_{rc}$). Under this condition, both layers are indistinguishable, and the measured phase shifts correspond to the bulk sensitivities $S^{TE}_T$ and $S^{TM}_T$. From these measured bulk sensitivities and the known interaction length, the corresponding waveguide sensitivities $S^{TE}_{wg,B}$ and $S^{TM}_{wg,B}$ can be derived through the architecture sensitivity. These values represent the response of the sensing waveguide to uniform RI changes and serve as a natural entry point for calibrating the sensor.

Importantly, these experimentally obtained sensitivities are used to define an equivalent waveguide: a numerical model whose geometry (e.g., width and height) is tuned so that the simulated waveguide sensitivities match the experimentally extracted values $S^{TE}_{wg,B}$ and $S^{TM}_{wg,B}$. This equivalent geometry effectively captures fabrication deviations (such as overetching, thickness variations, or refractive index inhomogeneities) using a simplified but physically meaningful parameterization based only on the effective width ($W$) and height ($H$).

Notably, multiple geometries may satisfy this condition; that is, different combinations of $W$ and $H$ can reproduce the experimental bulk sensitivity for both polarizations. These combinations are considered candidate geometries. However, these candidates can differ substantially in their evanescent field profiles, leading to different surface interactions. Therefore, the bulk calibration step alone is insufficient to uniquely determine the surface sensitivity behavior of the actual waveguide.

**Step 2: simulation-based estimation of surface overlap factors.** To resolve this ambiguity and identify the appropriate equivalent geometry, we simulate the surface response of each candidate waveguide by using the Lumerical FDE solver [52]. Specifically, we calculated the modal field overlap with a 10 nm-thick surface layer—i.e., the coefficients $\eta^{TE}$ and $\eta^{TM}$ of Eq. (3). These values were derived from simulated mode profiles using Eq. (2).

Then, to select the correct model, we compare the simulated ratio $(S^{TM}_{wg,B} \cdot \eta^{TM})/(S^{TE}_{wg,B} \cdot \eta^{TE})$ for each candidate combination of $W$ and $H$ with the experimental ratio of phase shifts $\Delta\varphi^{TM}/\Delta\varphi^{TE}$, obtained when injecting a BSA solution, which induces a surface-localized refractive index change ($\Delta n_{rc} \approx 0$, $\Delta n_p \neq 0$).

This second step is thus essential for validating the surface sensitivity of the model. The candidate geometry whose simulated surface response ratio best matches the measured BSA response is selected as the final equivalent waveguide. Its associated field distribution then provides reliable values for $\eta^{TE}$ and $\eta^{TM}$, enabling accurate decoupling of surface and bulk effects in subsequent measurements.

This hybrid calibration procedure relies solely on two well-controlled experimental steps—the injection of a uniform glycerol solution and the injection of a BSA solution—while avoiding the need for precise deposition of a fully characterized thin film.

## 5. Proof-of-concept experiment

To demonstrate the proof of concept of our layer discrimination approach, we performed a sequence of alternating injections of glycerol solutions and BSA. Part of the acquired data was used for sensor calibration, while the remainder was employed to retrieve RI variations in the surface and bulk layers, thus validating the full sensing and discrimination capability on a representative chip.

In every proof-of-concept experiment we use newly prepared chips that are cleaned following the same protocol to ensure controlled and reproducible surface properties. This is particularly important for adsorption-based measurements, where the interaction between BSA and the sensor surface is highly sensitive to local contamination, surface energy, or roughness [53,54].

From an application perspective, this experimental strategy is aligned with many integrated photonic biosensing platforms that operate with low-cost, single-use sensor chips (often embedded in disposable microfluidic cartridges), where a newly functionalized sensor is used for each assay or small set of assays [55,56]. In this single-use regime, demonstrating perfect recovery of the original baseline after multiple aggressive regeneration cycles is not critical. Instead, what matters is that the surface state remains stable over the duration of each calibration and measurement sequence. Strong alkaline cleaning solutions typically employed to remove adsorbed proteins (e.g., 1% v/v Tween in 0.12 M of NaOH [57]) are known to gradually modify $Si_3N_4$ surfaces. The extent of this surface evolution increases with base concentration and exposure time [58,59]. As a result, repeated NaOH-based regeneration steps would be expected to induce small, irreversible shifts of the interferometric baseline over successive cycles, making the single-use strategy particularly attractive for our proof-of-concept implementation.

The sequence of injections used in our proof-of-concept experiment consisted of: Water→ 6% Glycerol → Water→ 10 μg/mL BSA → Water→ 0.05% Glycerol → Water→ 0.5% Glycerol → Water→ 500 μg/mL BSA → Water→ 6% Glycerol → Water. BSA molecules adsorb onto the silicon nitride surface, inducing surface-localized RI changes, whereas glycerol uniformly modifies the bulk RI within the cladding region [60,61]. All BSA and glycerol solutions were prepared in deionized (Milli-Q) water at the concentrations indicated in the sequence, and this same water was used as the rinsing buffer between injections. The pH of these solutions was measured and found to be close to neutral (pH ≈ 7), which is a standard operating range for albumin and many other serum proteins in optical biosensing assays and is compatible with realistic biological detection conditions [62,63].

The corresponding phase shifts for both TE and TM modes over time are presented in Fig. 8(a). Notably, the phase shifts induced by the final 6% glycerol injection closely match those measured during the initial injection, confirming that the bulk refractive index response remains consistent throughout the experiment and validating the stability of the system.

The first two injections (6% Glycerol and 10 μg/mL BSA) are useful for calibration. As part of Step 1 the first injection of 6% Glycerol was used to experimentally determine bulk waveguide sensitivities $S^{TE}_{wg,B}$ and $S^{TM}_{wg,B}$. Since this injection produces a homogeneous refractive index increase in the cladding ($\Delta n_c = 6.9 \cdot 10^{-3}$ RIU), dividing the measured phase shifts by this known $\Delta n_c$ yields $S^{TE}_T = 7873.6\,\mathrm{rad/RIU}$ and $S^{TM}_T = 11825\,\mathrm{rad/RIU}$. These values reflect the overall response of each polarization mode to uniform RI changes and account for chip-specific fabrication variations. To incorporate these values into a numerical model, we compare the corresponding experimental waveguide sensitivities ($S^{TE}_{wg,B} = 0.1824\,\mathrm{RIU/RIU}$ and $S^{TM}_{wg,B} = 0.2739\,\mathrm{RIU/RIU}$) with numerical simulations over a sweep of waveguide widths ($W$) and heights ($H$). In Fig. 8(b), we plot the iso-sensitivity curves, i.e., the combinations of width ($W$) and height ($H$) for which the simulated sensitivities equal the experimentally measured values, for both the TE and TM modes. The intersection points of these curves indicate candidate waveguide geometries ($W_{eq}$, $H_{eq}$) that simultaneously satisfy the measured $S^{TE}_{wg,B}$ and $S^{TM}_{wg,B}$. In this case, two possible equivalent waveguides were found: ($W$ = 795 nm, $H$ = 333 nm) and ($W$ = 1015 nm, $H$ = 251 nm).

Proceeding to Step 2, we refine the choice of equivalent geometry by evaluating the sensor response to surface refractive index variations. While the bulk calibration step (Step 1) may yield more than one equivalent geometry that reproduces the same response to homogeneous RI

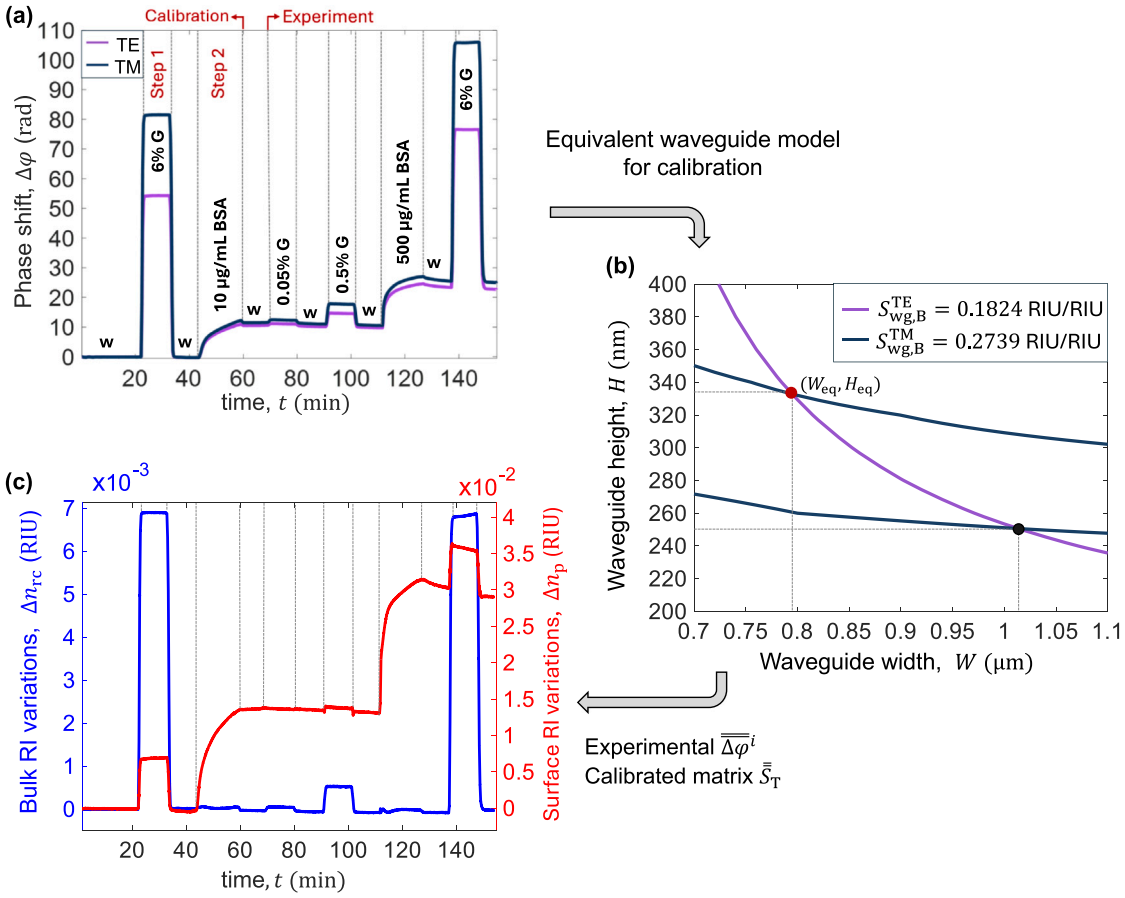


**Fig. 8.** Dual-polarization response, equivalent waveguide model, and reconstruction of layered refractive index variations. (a) Temporal phase response for TE (purple) and TM (dark blue) modes during different injections of glycerol (G) and bovine serum albumin (BSA) solutions in water (W); (b) Iso-sensitivity curves for TE and TM modes used to obtain the equivalent waveguide model and calibrate the sensitivity matrix; (c) Reconstructed RI variations in a 10 nm-thick surface layer (red) and in the remaining cladding region (blue) during the same injection sequence.

variations in the cover (Fig. 8(b)), the second calibration step removes this ambiguity. For each equivalent waveguide candidate obtained from the iso-sensitivity curves, we compute the values of $\eta^{TE}$ and $\eta^{TM}$ through the perturbational analysis considering a 10 nm-thick surface layer. From these values we derive the polarization-dependent surface-dominated response ratio, $\Delta\varphi^{TM}/\Delta\varphi^{TE}|_{surf} = (S^{TM}_{wg,B} \cdot \eta^{TM})/(S^{TE}_{wg,B} \cdot \eta^{TE})$. The corresponding geometries, overlap factors and ratios for the nominal design geometry and the main candidates are summarized in Table 1. Comparing these simulated ratios with the experimental phase shift ratio $\Delta\varphi^{TM}/\Delta\varphi^{TE} \approx 1.1$ observed upon surface-dominated modification—i.e., after the 10 µg/mL BSA injection in Fig. 8(a)—allows us to select geometry A ($W_{eq}$ = 795 nm, $H_{eq}$ = 333 nm) as the equivalent waveguide used in the subsequent analysis. This ensures that the chosen geometry not only reproduces the bulk behavior but also reflects the actual surface sensitivity response. Notably, this equivalent geometry lies within the fabrication tolerance margins specified by the foundry and reported in previous works based on the same photonic integration platform and supporting the consistency and physical plausibility of the extracted model [26,43]. In this way, the complete two-step calibration protocol is not ambiguous: it eliminates the non-uniqueness inherent to bulk-only fits and defines a unique, equivalent waveguide for subsequent inversion.

**Table 1**
Simulated surface overlap factors ($\eta^i$) and surface-dominated phase shift ratios ($\Delta\varphi^{TM}/\Delta\varphi^{TE}|_{surf}$) for three different waveguide geometries: nominal design, candidate A and candidate B. All values are computed for a 10 nm-thick virtual surface layer.

| Geometry | $W_{eq}$ (nm) | $H_{eq}$ (nm) | $\eta^{TE}$ | $\eta^{TM}$ | $\frac{\Delta\varphi^{TM}}{\Delta\varphi^{TE}}\|_{surf}$ |
|---|---|---|---|---|---|
| Nominal design | 1000 | 300 | 0.1003 | 0.0693 | 1.04 |
| Candidate A | 795 | 333 | 0.1003 | 0.0736 | 1.10 |
| Candidate B | 1015 | 251 | 0.0939 | 0.0617 | 0.99 |

The selected equivalent geometry ($W_{eq}$ = 795 nm, $H_{eq}$ = 333 nm), together with the previously calculated surface overlap factors $\eta^{TE}$ = 0.1003 and $\eta^{TM}$ = 0.0736, are used to construct the sensitivity matrix $\bar{\bar{S}}_T$ for the experiment. This matrix relates the observed phase shifts in both polarization modes to RI variations in the surface and bulk layers. Its condition number (≈ 70) ensures that the inversion is sufficiently well-conditioned to reliably separate both contributions.

Using this matrix and the experimental phase shifts shown in Fig. 8(a), we extract the RI changes in each layer throughout the injection sequence. As presented in Fig. 8(c), the first glycerol injection leads to a uniform RI increase of $6.9 \cdot 10^{-3}$ RIU, equally detected in both layers, thereby validating the bulk calibration (Step 1). The BSA injection yields a clear increase in RI observed in the layer closest to the surface, due to protein adsorption (Step 2). This confirms that BSA primarily affects the surface region. Additionally, a small refractive index change is also detected in the bulk region, since the BSA solution is not pure water and has a slightly increased refractive index.

One noticeable feature in the reconstructed RI variations is the apparent increase in the surface refractive index when glycerol solutions are injected after protein adsorption. In our model, $\Delta n_p$ is defined as an effective field-weighted RI change within a fixed near-surface region

of thickness $d_p = 10$ nm, not as the intrinsic RI of a compact protein film. Protein adlayers are typically hydrated and may not fully occupy this region [64,65], so part of the near-surface volume remains solvent-filled [38]. Therefore, a glycerol-induced bulk RI step can partially contribute to the effective near-surface index, even without further adsorption.

Moreover, previous studies report that a saturated monolayer of BSA exhibits a refractive index of approximately 1.42, leading to a RI variation of around 0.1 RIU relative to the buffer solution [38,66]. A saturated BSA monolayer is typically around 3 nm under saturation conditions [67–69]. Under our $d_p = 10$ nm definition, this corresponds to an average effective index increase of about $\Delta n_p \approx 0.1 \times 3/10 = 0.03$ RIU. Remarkably, this value aligns closely with the surface RI increment retrieved from the inversion procedure following the 500 μg/mL BSA injection—see Fig. 8(c). This agreement demonstrates that our method not only detects the presence of surface-bound biomolecules, but also quantitatively resolves their contribution to the optical response with high accuracy. In addition, we have verified that varying the assumed thickness of the surface recognition region within a realistic 3–10 nm range mainly rescales the retrieved surface index, while leaving the recovered bulk contribution and the qualitative separation between bulk and surface responses essentially unchanged (see Appendix C).

In this equivalent-waveguide framework, the main effect of fabrication tolerances in width, thickness and material indices is absorbed into the calibrated pair $(W_{eq}, H_{eq})$, which is fitted to the measured bulk and surface responses of the specific chip rather than to nominal dimensions. To assess the impact of residual mismatch between the true structure and this equivalent representation, we performed a local sensitivity study around the calibrated geometry $(W_{eq}, H_{eq}) = (795\ \text{nm}, 333\ \text{nm})$. We varied $W_{eq}$ by ±50 nm and $H_{eq}$ by ±15 nm. Then, we recomputed $\eta^{TE}$ and $\eta^{TM}$ and the retrieved indices for glycerol and BSA injections. These perturbations should be interpreted as conservative residual calibration errors around $(W_{eq}, H_{eq})$, not as additional process tolerances. Over these ranges, the relative changes in simulated $\eta^{TE}$ and $\eta^{TM}$ remain below about 1.5% and 3.2%, respectively. Furthermore, retrieved RI variations vary smoothly: glycerol remains clearly bulk-dominated and returns to baseline after rinsing, while BSA consistently shows an additional surface-localized contribution. Consequently, these residual errors do not compromise the qualitative separation between bulk- and surface-dominated responses.

To quantify the instrument resolution, we use drift-reduced baseline segments (≈ 30 s) and estimate short-term standard deviations of the retrieved refractive indices. For the calibrated device, the sensitivity matrix has a condition number $\kappa(\overline{\overline{S}}_{wg}) \approx 70$ and the short-term experimental noise levels are $\sigma_{\Delta n_p} \approx 1.2 \cdot 10^{-5}$ RIU and $\sigma_{\Delta n_{rc}} \approx 1.2 \cdot 10^{-6}$ RIU, which are in very good agreement with the covariance-based error-propagation analysis detailed in Appendix B. Using the conventional $3\sigma$ criterion, we estimate that RI variations as small as $4 \cdot 10^{-5}$ RIU can be reliably detected within the first 10 nm of the surface layer. In the bulk region, variations down to $4 \cdot 10^{-6}$ RIU can be resolved. Over the full proof-of-concept experiment (several hours), slow baseline drifts may occur. We mitigate these long-term trends with a simple linear baseline correction, which does not materially change the short-term (≈ 30 s) noise level used to compute the LODs above.

This provides a clear, quantitative benchmark of the sensor precision, underlining its ability to deliver robust, layer-resolved measurements in complex environments, which is an important advantage over conventional label-free biosensors. The underlying layer-discrimination mechanism is not specific to a particular analyte but is based on general optical conditions, namely the presence of a dielectric layer near the waveguide surface and different penetration depths and overlap factors for the TE and TM modes. These conditions are fulfilled by a wide range of biosensing coatings, so extending the present platform to additional biomolecular targets and to complex matrices such as diluted serum will primarily require adapting the biofunctionalization and antifouling strategies, rather than modifying the photonic transducer itself.

## 6. Conclusions

We have presented a dual-polarization interferometric approach capable of resolving refractive index changes occurring in different spatial regions, specifically at the surface and within the remaining bulk cladding of an integrated photonic sensor. By exploiting the inherent differences in sensitivity between TE and TM modes and applying perturbative analysis, we constructed a sensitivity matrix that enables the quantitative separation of these spatial contributions.

The proposed method was validated experimentally through alternating injections of BSA and glycerol solutions to modify the surface and bulk regions, respectively. The retrieved refractive index variations not only aligned with the expected physical behavior of these injections but also demonstrated excellent agreement with literature values for BSA monolayers, confirming the accuracy of the inversion model.

To the best of our knowledge, this is the first demonstration of spatially resolved refractive index discrimination separating surface-localized and bulk contributions within a compact, integrated photonic biosensor with coherent interrogation. For the 10 nm surface layer, the system can resolve RI changes as small as $4 \cdot 10^{-5}$ RIU, substantially reducing measurement uncertainty for surface-localized molecular interactions. This capability, not typically achievable with conventional label-free sensors, provides a critical advantage for the quantitative analysis of molecular interactions in multilayer or compositionally heterogeneous environments. As a result, it enables more accurate and informative biosensing in real-world applications.

## CRediT authorship contribution statement

**Ana Sánchez-Ramírez:** Writing – original draft, Validation, Software, Methodology, Investigation, Formal analysis, Conceptualization. **José Manuel Luque-González:** Writing – review & editing, Supervision, Formal analysis. **Laura Pérez-Sánchez:** Writing – review & editing, Resources, Methodology. **Miguel Barrio-Segura:** Resources, Methodology. **Érika López-Arroyo:** Visualization, Validation, Data curation. **Rafael Godoy-Rubio:** Formal analysis, Conceptualization. **Claudio J. Oton:** Writing – review & editing, Supervision, Resources, Methodology. **J. Gonzalo Wangüemert-Pérez:** Writing – review & editing, Supervision, Methodology, Conceptualization. **Íñigo Molina-Fernández:** Writing – review & editing, Supervision, Resources, Project administration, Funding acquisition, Formal analysis, Conceptualization.

## Declaration of competing interest

The authors declare the following financial interests/personal relationships that may be considered as potential competing interests:

J. Gonzalo Wangüemert-Perez and Íñigo Molina-Fernandez report a relationship with Bioherent S.L. that includes: equity or stocks. Ana Sánchez-Ramírez, Rafael Godoy Rubio, J. Gonzalo Wangüemert-Pérez and Íñigo Molina-Fernández have patent # ES20220030993, WO2024105300 “Integrated photonic biosensor with layer discrimination ability and coherent reading system, and device, assembly and methods associated with same” licensed to Bioherent S.L.

## Acknowledgments

We acknowledge funding from Ministerio de Ciencia e Innovación (PRE2020-096438, PID2019-106747RB-I00), Ministerio para la Transformación Digital y de la Función Pública (TSI-069100-2023-0013), Ministerio de Ciencia, Innovación y Universidades (MIG-20231023, PDC2023-145833-I00) and funding for open access charges: Universidad de Málaga/CBUA.

## Appendix A. Mathematical derivation of the multilayer sensitivity matrix

### A1. First-order perturbation theory

For a guided mode $i$ (TE or TM), the first-order perturbation expression for the effective-index change variation due to a small refractive-index perturbation $\Delta n(x, y)$ in the cladding can be written as [70,71]:

$$\Delta n^i_{\text{eff}} = \varepsilon_0 c\, n_c \frac{\iint_{R_{\text{total}}} \Delta n(x,y) \left|\overline{E}^i(x,y)\right|^2 dx\, dy,}{\iint_{R_{\text{total}}} \text{Re}\left\{\left(\overline{E}^i_t \times \overline{H}^{i*}_t\right)\cdot \hat{z}\right\} dx\, dy} \tag{A.1}$$

where $\overline{E}^i(x,y)$ is the unperturbed modal electric field, $\overline{E}^i_t$ and $\overline{H}^i_t$ are the transverse electric and magnetic field components, and $n_c$ is the reference-buffer refractive index used to compute the unperturbed mode.

Here, $R_{\text{total}}$ denotes the entire cross-section used for mode normalization (i.e., the full 2D simulation window), while $R_{\text{cover}}$ denotes the cover (top-cladding) region where the refractive-index perturbation is applied. Since $\Delta n(x, y) = 0$ outside the cover, the numerator integral can be restricted to $R_{\text{cover}}$ without loss of generality. For compactness, we define the constant

$$A^i = \frac{\varepsilon_0 c\, n_c}{\iint_{R_{\text{total}}} \text{Re}\left\{\left(\overline{E}^i_t \times \overline{H}^{i*}_t\right)\cdot \hat{z}\right\} dx\, dy}, \tag{A.2}$$

so that Eq. (A.1) becomes

$$\Delta n^i_{\text{eff}} = A^i \iint_{R_{\text{cover}}} \Delta n(x,y) \left|\overline{E}^i(x,y)\right|^2 dx\, dy. \tag{A.3}$$

Throughout this derivation, consistent with first-order perturbation, $\mathbf{E}^i(x, y)$ is the unperturbed field computed once for the reference buffer ($n_c$) and is kept fixed while evaluating sensitivities.

### A2. Conventional homogeneous (bulk) sensing

In the conventional bulk-sensing case, the perturbation is homogeneous across the entire cover,

$$\Delta n(x, y) = \Delta n_c \qquad \text{for all } (x, y) \in R_{\text{cover}}. \tag{A.4}$$

Substituting Eq. (A.4) into Eq. (A.3) yields

$$\Delta n^i_{\text{eff}} = A^i \left(\iint_{R_{\text{cover}}} \left|\overline{E}^i\right|^2 dx\, dy\right) \Delta n_c. \tag{A.5}$$

This motivates the definition of the conventional bulk sensitivity of mode $i$:

$$S^i_{\text{wg,B}} \equiv \frac{\Delta n^i_{\text{eff}}}{\Delta n_c} = A^i \iint_{R_{\text{cover}}} \left|\overline{E}^i\right|^2 dx\, dy. \tag{A.6}$$

### A3. Multilayer model and sensitivity matrix factorization

In our two-region model, the cover is split into two disjoint regions: a thin surface strip $R_p$ of thickness $d_p$ and the remaining cover $R_{rc}$ above it, such that

$$R_{\text{cover}} = R_p \cup R_{rc}, \qquad R_p \cap R_{rc} = \emptyset. \tag{A.7}$$

Accordingly, the cover overlap integral satisfies

$$\iint_{R_{\text{cover}}} \left|\overline{E}^i\right|^2 dx\, dy = \iint_{R_p} \left|\overline{E}^i\right|^2 dx\, dy + \iint_{R_{rc}} \left|\overline{E}^i\right|^2 dx\, dy. \tag{A.8}$$

We assume the perturbation is piecewise constant:

$$\Delta n(x, y) = \begin{cases} \Delta n_p, & (x, y) \in R_p, \\ \Delta n_{rc}, & (x, y) \in R_{rc}. \end{cases} \tag{A.9}$$

Substituting Eq. (A.9) into Eq. (A.3) and splitting the integral yields

$$\Delta n^i_{\text{eff}} = A^i \left[\Delta n_p \iint_{R_p} \left|\overline{E}^i\right|^2 dx\, dy + \Delta n_{rc} \iint_{R_{rc}} \left|\overline{E}^i\right|^2 dx\, dy\right]. \tag{A.10}$$

We then define the total cover overlap as

$$C^i = \iint_{R_{\text{cover}}} \left|\overline{E}^i\right|^2 dx\, dy. \tag{A.11}$$

By multiplying and dividing Eq. (A.10) by $C_i$ gives

$$\Delta n^i_{\text{eff}} = A^i C^i \left[\left(\frac{\iint_{R_p} \left|\overline{E}^i\right|^2 dx\, dy}{C^i}\right) \Delta n_p + \left(\frac{\iint_{R_{rc}} \left|\overline{E}^i\right|^2 dx\, dy}{C^i}\right) \Delta n_{rc}\right]. \tag{A.12}$$

We now define the surface overlap factor and the remaining-cover fraction using Eq. (A.8):

$$\eta^i = \frac{\iint_{R_p} \left|\overline{E}^i\right|^2 dx\, dy}{\iint_{R_{\text{cover}}} \left|\overline{E}^i\right|^2 dx\, dy} = \frac{\iint_{R_p} \left|\overline{E}^i\right|^2 dx\, dy}{C^i}. \tag{A.13}$$

$$1 - \eta^i = \frac{\iint_{R_{rc}} \left|\overline{E}^i\right|^2 dx\, dy}{C^i} \tag{A.14}$$

Substituting Eqs. (A.13) and (A.14) into Eq. (A.12) yields

$$\Delta n^i_{\text{eff}} = A^i C^i \left[\eta^i \Delta n_p + (1 - \eta^i)\Delta n_{rc}\right]. \tag{A.15}$$

Finally, by comparing Eq. (A.6) with Eq. (A.11), we identify $A^i C^i = S^i_{\text{wg,B}}$. Therefore,

$$\Delta n^i_{\text{eff}} = S^i_{\text{wg,B}} \left[\eta^i \Delta n_p + (1 - \eta^i)\Delta n_{rc}\right], \tag{A.16}$$

which directly implies the factorized partial sensitivities used in Eq. (1) of the main text:

$$\frac{\partial n^i_{\text{eff}}}{\partial n_p} = \eta^i\, S^i_{\text{wg,B}}, \qquad \frac{\partial n^i_{\text{eff}}}{\partial n_{rc}} = (1 - \eta^i)\, S^i_{\text{wg,B}}. \tag{A.17}$$

Considering both the TE and TM modes, Eq. (A.17) leads to the waveguide sensitivity matrix factorization used in the manuscript (Eq. 3):

$$\overline{\overline{S}}_{\text{WG}} = \begin{bmatrix} S^{\text{TE}}_{\text{wg,B}} & 0 \\ 0 & S^{\text{TM}}_{\text{wg,B}} \end{bmatrix} \begin{bmatrix} \eta^{\text{TE}} & 1 - \eta^{\text{TE}} \\ \eta^{\text{TM}} & 1 - \eta^{\text{TM}} \end{bmatrix}. \tag{A.18}$$

## Appendix B. Covariance-based noise propagation analysis

The dual-parameter inversion can be written in compact matrix form as

$$\overline{\Delta\varphi} = \overline{\overline{S}}_{\text{T}} \overline{\Delta n}, \qquad \overline{\Delta\varphi} = \begin{bmatrix} \Delta\varphi^{\text{TE}} \\ \Delta\varphi^{\text{TM}} \end{bmatrix}, \quad \overline{\Delta n} = \begin{bmatrix} \Delta n_p \\ \Delta n_{rc} \end{bmatrix}, \tag{B.1}$$

where $\Delta n_p$ and $\Delta n_{rc}$ denote the effective surface and residual-cover refractive index changes, respectively, and $\overline{\overline{S}}_{\text{T}}$ is the $2 \times 2$ total sensitivity

matrix defined in Section 2. The refractive index changes are retrieved as

$$\overline{\Delta n} = \overline{\overline{K}}\,\overline{\Delta\varphi}, \qquad \overline{\overline{K}} = \overline{\overline{S}}_{\mathrm{T}}^{-1}. \tag{B.2}$$

Small phase fluctuations $\varepsilon_{\overline{\Delta\varphi}}$ around a given operating point are mapped linearly to index fluctuations,

$$\varepsilon_{\overline{\Delta n}} = \overline{\overline{K}}\,\varepsilon_{\overline{\Delta\varphi}}. \tag{B.3}$$

The phase-noise statistics are described by the 2×2 covariance matrix

$$\mathrm{cov}(\varepsilon_{\overline{\Delta\varphi}}) = \begin{bmatrix} \sigma^2_{\Delta\varphi^{\mathrm{TE}}} & \rho\,\sigma_{\Delta\varphi^{\mathrm{TE}}}\sigma_{\Delta\varphi^{\mathrm{TM}}} \\ \rho\,\sigma_{\Delta\varphi^{\mathrm{TE}}}\sigma_{\Delta\varphi^{\mathrm{TM}}} & \sigma^2_{\Delta\varphi^{\mathrm{TM}}} \end{bmatrix}, \tag{B.4}$$

where $\sigma_{\Delta\varphi^{\mathrm{TE}}}$ and $\sigma_{\Delta\varphi^{\mathrm{TM}}}$ are the TE/TM phase standard deviations and $\rho$ is their correlation coefficient.

For a linear mapping, the covariance of the retrieved indices follows the standard transformation rule from multivariate statistics and uncertainty analysis [72,73]:

$$\mathrm{cov}(\varepsilon_{\overline{\Delta n}}) = \overline{\overline{K}}\;\mathrm{cov}(\varepsilon_{\overline{\Delta\varphi}})\;\overline{\overline{K}}^{T}. \tag{B.5}$$

The diagonal elements of $\mathrm{cov}(\overline{\varepsilon_n})$ provide the variances $\sigma^2_{\Delta n_p}$ and $\sigma^2_{\Delta n_{rc}}$. Denoting by $K_{ij}$ the elements of the inversion matrix $\overline{\overline{K}}$, these variances can be written explicitly as

$$\sigma^2_{\Delta n_p} = K_{11}^2\sigma^2_{\Delta\varphi^{\mathrm{TE}}} + K_{12}^2\sigma^2_{\Delta\varphi^{\mathrm{TM}}} + 2K_{11}K_{12}\,\rho\,\sigma_{\Delta\varphi^{\mathrm{TE}}}\,\sigma_{\Delta\varphi^{\mathrm{TM}}}, \tag{B.6}$$

$$\sigma^2_{\Delta n_{rc}} = K_{21}^2\sigma^2_{\Delta\varphi^{\mathrm{TE}}} + K_{22}^2\sigma^2_{\Delta\varphi^{\mathrm{TM}}} + 2K_{21}K_{22}\,\rho\,\sigma_{\Delta\varphi^{\mathrm{TE}}}\,\sigma_{\Delta\varphi^{\mathrm{TM}}}. \tag{B.7}$$

In the experiments, $\sigma_{\Delta\varphi^{\mathrm{TE}}}$, $\sigma_{\Delta\varphi^{\mathrm{TM}}}$ and $\rho$ are estimated from drift-reduced baseline segments of ≈ 30 s without sample injection, and inserted into (B.6) and (B.7) to obtain the standard deviations $\sigma_{\Delta n_{\mathrm{p}}}$ and $\sigma_{\Delta n_{\mathrm{rc}}}$. These values coincide, within experimental uncertainty, with the standard deviations obtained directly from the reconstructed $\Delta n_{\mathrm{p}}(t)$ and $\Delta n_{\mathrm{rc}}(t)$ traces over the same baseline segments. Using the conventional $3\sigma$ criterion, the corresponding detection limits for a 10 nm-thickness layer reported in Section 5 are $\mathrm{LOD}_{\Delta n_{\mathrm{p}}} \approx 4\times10^{-5}$ RIU and $\mathrm{LOD}_{\Delta n_{\mathrm{rc}}} \approx 4\times10^{-6}$ RIU.

## Appendix C. Effect of recognition layer thickness

To assess the impact of the assumed recognition-layer thickness, we recalculated the TE/TM surface overlaps ($\eta^{\mathrm{TE}}$ and $\eta^{\mathrm{TM}}$) and re-analyzed the BSA/glycerol proof-of-concept dataset for three representative values of the effective surface thickness, $d_{\mathrm{p}}$ = 10 nm, 5 nm and 3 nm. In this thin-film regime, the surface overlaps ($\eta^i$) of both polarizations increase approximately linearly with $d_{\mathrm{p}}$, while the qualitative bulk/surface separation remains unchanged: glycerol is consistently retrieved as a predominantly bulk perturbation, and BSA as a predominantly surface perturbation.

The corresponding noise levels of the retrieved indices are consistent with this thickness dependence. The short-term standard deviation of the surface refractive index increases from $\sigma_{\Delta n_{\mathrm{p}}} \approx 1.2\cdot10^{-5}$ RIU (for 10 nm-layer thickness) to $\approx 4.3\cdot10^{-5}$ RIU (for 3 nm-layer thickness), whereas the bulk index noise remains essentially constant at $\sigma_{\Delta n_{\mathrm{rc}}} \approx 1.3\cdot10^{-6}$ RIU. As illustrated in Fig. C.1, the bulk contribution is practically unaffected by the choice of $d_{\mathrm{p}}$, and the surface contribution associated with BSA remains clearly above the noise level and is only rescaled in amplitude. These results confirm that, within the realistic 3–10 nm range, the choice of $d_{\mathrm{p}}$ mainly changes the normalization of the effective surface index without altering the recovered bulk contribution or the qualitative bulk/surface discrimination.

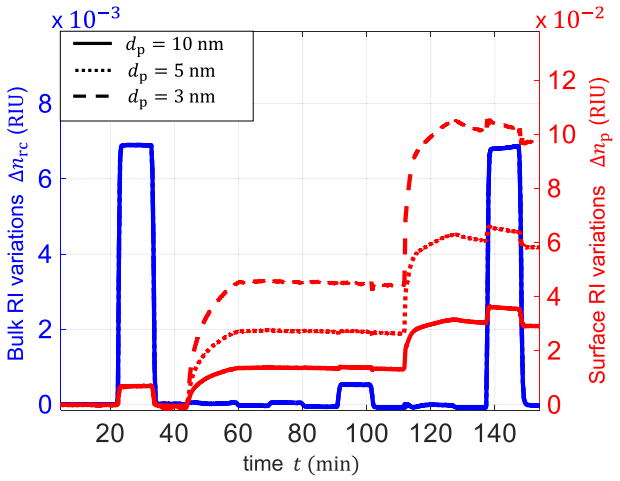


**Fig. C.1.** Effect of the assumed recognition-layer thickness on the retrieved indices. Retrieved bulk ($\Delta n_{\mathrm{rc}}$) and surface ($\Delta n_{\mathrm{p}}$) refractive-index changes when the effective surface thickness is set to $d_{\mathrm{p}}$ = 10 nm, 5 nm and 3 nm.

## Data availability

The data that has been used is confidential.

## References

[1] A. Haleem, M. Javaid, R. Singh, R. Suman, S. Rab, Biosensors applications in medical field: a brief review, Sens. Int. 2 (2021) 100100, https://doi.org/10.1016/j.sintl.2021.100100

[2] S. Nath, Advancements in food quality monitoring: integrating biosensors for precision detection, Sustain. Food Technol. 2 (2024) 976–992, https://doi.org/10.1039/D4FB00094C

[3] A. Tsalsabila, V. Alphano Dabur, I. Budiarso, S. Wustoni, H.-C. Chen, M.D. Birowosuto, A. Wibowo, S. Zeng, Progress and outlooks in designing photonic biosensor for virus detection, Adv. Opt. Mater. 12 (Jul 2024), https://doi.org/10.1002/adom.202400849

[4] A. La Grasta, M.I. Gómez-Gómez, A. Griol, M. De Carlo, V.M.N. Passaro, A. Martínez, F. Dell'Olio, Performance assessment of silicon nitride ring resonators for biosensing applications, in: 2024 24th International Conference on Transparent Optical Networks (ICTON), 2024, pp. 1–4, https://doi.org/10.1109/ICTON62926.2024.10647624

[5] K.A. Buzaverov, A.S. Baburin, E.V. Sergeev, S.S. Avdeev, E.S. Lotkov, S.V. Bukatin, I.A. Stepanov, A.B. Kramarenko, A.S. Amiraslanov, D.V. Kushnev, I.A. Ryzhikov, I.A. Rodionov, Silicon nitride integrated photonics from visible to mid-infrared spectra, Laser Photonics Rev. 18 (12) (2024) 2400508, https://doi.org/10.1002/lpor.202400508

[6] A. Sánchez-Ramírez, J.M. Luque-González, J.G. Wangüemert-Pérez, A. Ortega-Moñux, Í. Molina-Fernández, Comparing dielectric and plasmonic waveguides in a Mach-Zehnder architecture with coherent readout for sensing applications, Opt. Laser Technol. 168 (2024) 109813, https://doi.org/10.1016/j.optlastec.2023.109813

[7] S. Hassan, C. Schreib, X. Zhao, G. Duret, D. Roman, V. Nair, T. Cohen-Karni, O. Veiseh, J. Robinson, Real-time in vivo sensing of nitric oxide using photonic microring resonators, ACS Sensors 7 (Aug 2022), https://doi.org/10.1021/acssensors.2c00756

[8] A. la Grasta, M. De Carlo, N. Ardoino, R. Favaretto, F. Labbé, Y. Ding, V.M.N. Passaro, F. Dell'Olio, Silicon-on-insulator microphotonic resonators for label-free biosensing: an experiment-based comparison between the different configurations, IEEE Sens. J. 24 (14) (2024) 22351–22358, https://doi.org/10.1109/JSEN.2024.3406945

[9] C. Dhote, A. Singh, S. Kumar, Silicon photonics sensors for biophotonic applications—a review, IEEE Sens. J. 22 (19) (2022) 18228–18239, https://doi.org/10.1109/JSEN.2022.3199663

[10] J. Leuermann, V. Stamenkovic, P. Ramirez-Priego, A. Sánchez-Postigo, A. Fernández-Gavela, C.A. Chapman, R.C. Bailey, L.M. Lechuga, E. Perez-Inestrosa, D. Collado, R. Halir, I. Molina-Fernández, Coherent silicon photonic interferometric biosensor with an inexpensive laser source for sensitive label-free immunoassays, Opt. Lett. 45 (24) (2020) 6595–6598, https://doi.org/10.1364/OL.411635

[11] F. Vogelbacher, T. Kothe, P. Muellner, E. Melnik, M. Sagmeister, J. Kraft, R. Hainberger, Waveguide Mach-Zehnder biosensor with laser diode pumped integrated single-mode silicon nitride organic hybrid solid-state laser, Biosens. Bioelectron. 197 (2022) 113816, https://doi.org/10.1016/j.bios.2021.113816

[12] J.C. Ramirez, D. Grajales García, J. Maldonado, A. Fernández-Gavela, Current trends in photonic biosensors: advances towards multiplexed integration, Chemosensors 10 (10) (2022), https://doi.org/10.3390/chemosensors10100398

[13] M.A. Butt, Integrated optics: conventional mach–zehnder interferometer configuration versus loop terminated mach–zehnder interferometer configuration–a perspective, J. Opt. 26 (10) (2024) 102501, https://doi.org/10.1088/2040-8986/ad7515
[14] P.J. Reyes-Iglesias, I. Molina-Fernández, A. Moscoso-Mártir, A. Ortega-Moñux, High-performance monolithically integrated 120° downconverter with relaxed hardware constraints, Opt. Express 20 (5) (2012) 5725–5741, https://doi.org/10.1364/OE.20.005725
[15] I. Molina-Fernández, J. Leuermann, A. Ortega-Moñux, J.G. Wangüemert-Pérez, R. Halir, Fundamental limit of detection of photonic biosensors with coherent phase read-out, Opt. Express 27 (9) (2019) 12616–12629, https://doi.org/10.1364/OE.27.012616
[16] H. Erickson, Size and shape of protein molecules at the nanometer level determined by sedimentation, gel filtration, and electron microscopy, Biol. Proced. Online 11 (2009) 32–51, https://doi.org/10.1007/s12575-009-9008-x
[17] L. Castelló-Pedrero, M.I. Gómez-Gómez, J. García-Rupérez, A. Griol, A. Martínez, Performance improvement of a silicon nitride ring resonator biosensor operated in the TM mode at 1310 NM, Biomed. Opt. Express 12 (11) (2021) 7244–7260, https://doi.org/10.1364/BOE.437823
[18] F. Liu, X. Zhang, K. Li, T. Guo, A. Ianoul, J. Albert, Discrimination of bulk and surface refractive index change in plasmonic sensors with narrow bandwidth resonance combs, ACS Sensors 6 (8) (2021) 3013–3023, pMID: 34190543. https://doi.org/10.1021/acssensors.1c00906
[19] Q. Du, Q. Zhang, G. Liu, Multiple solution solving in plasmon sensing by deep learning: determination of a layer refractive index and thickness in one experiment, Opt. Lett. 46 (22) (2021) 5667–5670, https://doi.org/10.1364/OL.444442
[20] A. Amani, H. Kamyab, E. Vafa, A. Jahanbin, M. Abbasi, A. Vaez, G. Munuswamy-Ramanujam, R. Balasubramani, L. Gnanasekaran, D. Rocchio, M. Yusuf, Multifunctional mxenes nanocomposite platforms for biosensing and wearable sensor technologies, Adv. Compos. Hybrid Mater. 8 (Dec 2024), https://doi.org/10.1007/s42114-024-01118-8
[21] A. Kumar, A. Kumar, P. Sagar, M. Srivastava, A. Pandey, R. Prakash, S.K. Srivastava, A sensitive SPR biosensor for glucose detection using mos2 quantum dots, Microchem. J. 214 (2025) 113889, https://doi.org/10.1016/j.microc.2025.113889
[22] A. Frutiger, A. Tanno, S. Hwu, R. Tiefenauer, J. Vörös, N. Nakatsuka, Nonspecific binding—fundamental concepts and consequences for biosensing applications, Chem. Rev. 121 (Jun 2021), https://doi.org/10.1021/acs.chemrev.1c00044
[23] R.E. Shamy, M. Swillam, X. Li, On-chip sensing system employing wavelength splitting for noise suppression, J. Lightw. Technol. 43 (11) (2025) 5292–5298, https://doi.org/10.1109/JLT.2025.3549774
[24] S. Chen, Y. Liu, Q. Yu, W. Peng, Self-referencing SPR biosensing with an ultralow limit-of-detection using long-wavelength excitation, Sens. Actuators B: Chem. 327 (2021) 128935, https://doi.org/10.1016/j.snb.2020.128935
[25] R. Li, L. Yu, J. Li, W. Li, Y. Feng, J. Wang, X. Xu, Sensitivity enhancement of bimodal waveguide interferometric sensor based on regional mode engineering, Opt. Express 32 (6) (2024) 10274–10283, https://doi.org/10.1364/OE.519015
[26] A. Torres-Cubillo, J.M. Luque-González, A. Sánchez-Postigo, A. Fernández-Gavela, J.G. Wangüemert-Pérez, Í. Molina-Fernández, R. Halir, High-performance bimodal evanescent-field sensor with coherent phase readout, J. Lightwave Technol. 42 (8) (2024) 3010–3015, https://doi.org/10.1109/JLT.2023.3342476
[27] C. Worth, B.B. Goldberg, M. Ruane, M. Selim Unlu, Surface desensitization of polarimetric waveguide interferometers, IEEE J. Sel. Top. Quantum Electron. 7 (6) (2001) 874–877, https://doi.org/10.1109/2944.983287
[28] J. Escorihuela, M.Á. González-Martínez, J.L. López-Paz, R. Puchades, Á. Maquieira, D. Giménez-Romero, Dual-polarization interferometry: a novel technique to light up the nanomolecular world, Chem. Rev. 115 (1) (2015) 265–294, pMID: 25456305. https://doi.org/10.1021/cr5002063
[29] H.K.P. Mulder, C. Blum, V. Subramaniam, J.S. Kanger, Size-selective analyte detection with a young interferometer sensor using multiple wavelengths, Opt. Express 24 (8) (2016) 8594–8619, https://doi.org/10.1364/OE.24.008594
[30] C. Stamm, R. Dangel, W. Lukosz, Biosensing with the integrated-optical difference interferometer: dual-wavelength operation, Opt. Commun. 153 (4) (1998) 347–359, https://doi.org/10.1016/S0030-4018(98)00194-1
[31] S. Kedenburg, M. Vieweg, T. Gissibl, H. Giessen, Linear refractive index and absorption measurements of nonlinear optical liquids in the visible and near-infrared spectral region, Opt. Mater. Express 2 (11) (2012) 1588–1611, https://doi.org/10.1364/OME.2.001588
[32] J. Homola (Ed), Surface Plasmon Resonance Based Sensors, Vol. 4 of Springer Series on Chemical Sensors and Biosensors, Springer, Berlin Heidelberg, 2006, https://doi.org/10.1007/b100321
[33] B. Kovacs, R. Horváth, Modeling of label-free optical waveguide biosensors with surfaces covered partially by vertically homogeneous and inhomogeneous films, J. Sensors 2019 (2019) 1762450:1–1762450:11.
[34] A. Saftics, S. Kurunczi, B. Peter, I. Szekacs, J.J. Ramsden, R. Horvath, Data evaluation for surface-sensitive label-free methods to obtain real-time kinetic and structural information of thin films: a practical review with related software packages, Adv. Colloid Interface Sci. 294 (2021) 102431, https://doi.org/10.1016/j.cis.2021.102431
[35] K. Izuka, Perturbation theory (appx. B), in: Elements of Photonics, Volume II: for Fiber and Integrated Optics, Wiley Interscience, New York, 2002.
[36] F. Rana, Integrated optical waveguides (Ch. 8), in: Semiconductor Optoelectronics (ECE 5330 lecture notes), Cornell University, 2026. Available at: https://courses.cit.cornell.edu/ece533/Lectures/handout8.pdf (Accessed 11 Feb 2026).
[37] J.G. Wangüemert-Pérez, A. Hadij-ElHouati, A. Sánchez-Postigo, J. Leuermann, D.-X. Xu, P. Cheben, A. Ortega-Moñux, R. Halir, Í. Molina-Fernández, [invited] subwavelength structures for silicon photonics biosensing, Opt. Laser Technol. 109 (2019) 437–448, https://doi.org/10.1016/j.optlastec.2018.07.071
[38] J. Vörös, The density and refractive index of adsorbing protein layers, Biophys. J. 87 (1) (2004) 553–561, https://doi.org/10.1529/biophysj.103.030072
[39] L.N. Trefethen, D. Bau, III, Numerical Linear Algebra, Society for Industrial and Applied Mathematics, Philadelphia, PA, 1997, https://doi.org/10.1137/1.9780898719574
[40] G.H. Golub, C.F. van Loan, Matrix Computations, fourth ed, JHU Press, 2013.
[41] X. Li, H. Zhang, N. Chen, Y. Wang, X. Gao, X. Zhou, Simultaneous detection of magnetic field and temperature using micro-nanofiber cascaded fiber bragg grating structure, IEEE Sens. J. 22 (20) (2022) 19267–19272, https://doi.org/10.1109/JSEN.2022.3192179
[42] R. Halir, L. Vivien, X. Le Roux, D.-X. Xu, P. Cheben, Direct and sensitive phase readout for integrated waveguide sensors, IEEE Photon. J. 5 (4) (2013) 6800906, https://doi.org/10.1109/JPHOT.2013.2276747
[43] CORNERSTONE, Silicon photonics prototyping foundry, 2026, https://cornerstone.sotonfab.co.uk/ (Accessed 11 Feb 2026).
[44] I.H. Malitson, Interspecimen comparison of the refractive index of fused silica, J. Opt. Soc. Am. 55 (10) (1965) 1205–1209, https://doi.org/10.1364/JOSA.55.001205
[45] H.H. Li, Refractive index of silicon and germanium and its wavelength and temperature derivatives, J. Phys. Chem. Ref. Data 9 (3) (1980) 561–658, https://doi.org/10.1063/1.555624
[46] R.L. Bunch, D.I. Sanderson, S. Raman, Quality factor and inductance in differential IC implementations, IEEE Microw. Mag. 3 (2) (2002) 82–92, https://doi.org/10.1109/MMW.2002.1004055
[47] W. Bogaerts, L. Chrostowski, Silicon photonics circuit design: methods, tools and challenges, Laser Photon. Rev. 12 (4) (2018) 1700237, https://doi.org/10.1002/lpor.201700237
[48] F. Piretta, F. Samà, F. Bontempi, J. Elaskar, D. Angeloni, C.J. Oton, Interferometer-based chemical sensor on chip with enhanced responsivity and low-cost interrogation, Biomed. Opt. Express 15 (2024) 2767–2779, https://doi.org/10.1364/BOE.520195
[49] J.E. Saunders, C. Sanders, H. Chen, H.-P. Loock, Refractive indices of common solvents and solutions at 1550 nm, Appl. Opt. 55 (4) (2016) 947–953, https://doi.org/10.1364/AO.55.000947
[50] Z. Cao, L. Jiang, S. Wang, M. Wang, D. Liu, P. Wang, F. Zhang, Y. Lu, All-glass extrinsic Fabry-Perot interferometer thermo-optic coefficient sensor based on a capillary bridged two fiber ends, Appl. Opt. 54 (9) (2015) 2371–2375, https://doi.org/10.1364/AO.54.002371
[51] H. Qiu, C. Zhao, X. Hu, H. Chen, Q. Yu, Z. Lian, H. Qu, Glycerol–water solution-assisted mach–zehnder temperature sensor in specialty fiber with two cores and one channel, Photonics 8 (4) (2021), https://doi.org/10.3390/photonics8040103
[52] Lumerical, Ansys Lumerical photonic simulation software suite, 2026, https://www.lumerical.com/ (Accessed 11 Feb 2026).
[53] S. Sarkar, S. Kundu, structure and morphology of adsorbed protein (BSA) layer on hydrophilic silicon surface in presence of mono-, DI- and tri-valent ions, JCIS Open 3 (2021) 100016, https://doi.org/10.1016/j.jciso.2021.100016
[54] S. Sarkar, S. Kundu, Protein (BSA) adsorption on hydrophilic and hydrophobic surfaces, Materials Today: Proceedings (May 2023), https://doi.org/10.1016/j.matpr.2023.04.200
[55] J.S. Cognetti, D.J. Steiner, M. Abedin, M.R. Bryan, C. Shanahan, N. Tokranova, E. Young, A.M. Klose, A. Zavriyev, N. Judy, B. Piorek, C. Meinhart, R. Jakubowicz, H. Warren, N.C. Cady, B.L. Miller, Disposable photonics for cost-effective clinical bioassays: application to Covid-19 antibody testing, Lab Chip 21 (2021) 2913–2921, https://doi.org/10.1039/D1LC00369K
[56] D. Martens, P. Ramirez-Priego, M.S. Murib, A.A. Elamin, A.B. Gonzalez-Guerrero, M. Stehr, F. Jonas, B. Anton, N. Hlawatsch, P. Soetaert, R. Vos, A. Stassen, S. Severi, W. Van Roy, R. Bockstaele, H. Becker, M. Singh, L. Lechuga, P. Bienstman, A low-cost integrated biosensing platform based on sin nanophotonics for biomarker detection in urine, Anal. Methods 10 (2018) 3066–3073, https://doi.org/10.1039/C8AY00666K
[57] T. Wangkam, S. Yodmongkol, J. Disrattakit, B. Sutapun, R. Amarit, A. Somboonkaew, T. Srikhirin, Adsorption of bovine serum albumin (bsa) on polystyrene (PS) and its acid copolymer, Curr. Appl. Phys. 12 (1) (2012) 44–52, https://doi.org/10.1016/j.cap.2011.04.039
[58] L. Qiu, D.A. Guzonas, J. Qian, Corrosion of silicon nitride in high temperature alkaline solutions, J. Nucl. Mater. 476 (2016) 293–301, https://doi.org/10.1016/j.jnucmat.2016.04.056
[59] K. Bae, K. Lee, Restricted hydrolysis reaction of si3n4 via nonionic polymer adsorption in advanced shallow trench isolation chemical mechanical planarization, Colloids Surf. A: Physicochem. Eng. Asp. 681 (2024) 132716, https://doi.org/10.1016/j.colsurfa.2023.132716
[60] G. Ma, A. Ferhan, J. Jackman, N. Cho, Conformational flexibility of fatty acid-free bovine serum albumin proteins enables superior antifouling coatings, Commun. Mater. 1 (Jul 2020), https://doi.org/10.1038/s43246-020-0047-9
[61] A. Ferhan, Y. Hwang, M.S. Ibrahim, S. Anand, A. Kim, J. Jackman, N. Cho, Ultrahigh surface sensitivity of deposited gold nanorod arrays for nanoplasmonic biosensing, Appl. Mater. Today 23 (2021) 101046, https://doi.org/10.1016/j.apmt.2021.101046
[62] N.E. Kadi, N. Taulier, J.-Y. Le Huérou, M. Gindre, W. Urbach, I.J. Nwigwe, P.C. Kahn, M. Waks, Unfolding and refolding of bovine serum albumin at acid ph: ultrasound and structural studies, Biophys. J. 91 9 (2006) 3397–3404.
[63] P. Khramtsov, M. Kropaneva, M. Bochkova, V. Timganova, D. Kiselkov, S. Zamorina, M. Rayev, Synthesis and application of albumin nanoparticles loaded

with prussian blue nanozymes, Colloids Interfaces 6 (2) (2022), https://doi.org/10.3390/colloids6020029
[64] X. Wang, G. Herting, I. Odnevall Wallinder, E. Blomberg, Adsorption of bovine serum albumin on silver surfaces enhances the release of silver at ph neutral conditions, Phys. Chem. Chem. Phys. 17 (2015) 18524–18534, https://doi.org/10.1039/C5CP02306H
[65] P. Tworek, K. Rakowski, M. Szota, M. Lekka, B. Jachimska, Changes in secondary structure and properties of bovine serum albumin as a result of interactions with gold surface, ChemPhysChem 25 (2) (2024) e202300505, https://doi.org/10.1002/cphc.202300505
[66] N.J. Freeman, L.L. Peel, M.J. Swann, G.H. Cross, A. Reeves, S. Brand, J.R. Lu, Real time, high resolution studies of protein adsorption and structure at the solid–liquid interface using dual polarization interferometry, J. Phys. Condens. Matter 16 (26) (2004) S2493, https://doi.org/10.1088/0953-8984/16/26/023
[67] Y.L. Jeyachandran, E. Mielczarski, B. Rai, J.A. Mielczarski, Quantitative and qualitative evaluation of adsorption/desorption of bovine serum albumin on hydrophilic and hydrophobic surfaces, Langmuir 25 (19) (2009) 11614–11620, pMID: 19788219. https://doi.org/10.1021/la901453a
[68] T.J. Su, J.R. Lu, R.K. Thomas, Z.F. Cui, Effect of ph on the adsorption of bovine serum albumin at the silica/water interface studied by neutron reflection, J. Phys. Chem. B 103 (18) (1999) 3727–3736, https://doi.org/10.1021/jp983580j
[69] T.J. Su, J.R. Lu, R.K. Thomas, Z.F. Cui, J. Penfold, The conformational structure of bovine serum albumin layers adsorbed at the silica-water interface, J. Phys. Chem. B 102 (41) (1998) 8100–8108, https://doi.org/10.1021/jp981239t
[70] P. Berini, Bulk and surface sensitivities of surface plasmon waveguides, New J. Phys. 10 (2008) 105010, https://doi.org/10.1088/1367-2630/10/10/105010
[71] J. Milvich, D. Kohler, W. Freude, C. Koos, Surface sensing with integrated optical waveguides: a design guideline, Opt. Express 26 (2018) 19885–19906, https://doi.org/10.1364/OE.26.019885
[72] V. Kargin, Lecture Notes for the Linear Algebra for Statisticians (Math 530), Department of Mathematics and Statistics, Binghamton University, Lecture notes, Dec. 4, 2020. Available at: https://www2.math.binghamton.edu/lib/exe/fetch.php/people/kargin/publications/lnmath530_master.pdf (Accessed 11 Feb 2026).
[73] V. Yadav, S. Ghosh, C.E. Miller, Metrics for evaluating the quality in linear atmospheric inverse problems: a case study of a trace gas inversion, Geosci. Model Dev. 16 (17) (2023) 5219–5236, https://doi.org/10.5194/gmd-16-5219-2023